Progress in Oceanography 217 (2023) 103079

Contents lists available at ScienceDirect

Progress in Oceanography

journal homepage: www.elsevier.com/locate/pocean

Rapid fCO_2 rise in the northern Barents Sea and Nansen Basin

Ylva Ericson [a,*], Agneta Fransson [a,b], Melissa Chierici [c], Elizabeth M. Jones [c], Ingunn Skjelvan [d], Abdirahman Omar [d], Are Olsen [e,f], Meike Becker [e,f]

[a] Norwegian Polar Institute, Tromsø, Norway
[b] University Centre in Svalbard, Longyearbyen, Norway
[c] Institute of Marine Research, Tromsø, Norway
[d] NORCE Norwegian Research Centre, Bjerknes Center for Climate Research, Bergen, Norway
[e] Geophysical Institute, University of Bergen, Bergen, Norway
[f] Bjerknes Center for Climate Research, Bergen, Norway

ARTICLE INFO

Keywords:
Surface water fCO_2
Sea ice loss
Atlantification
Barents Sea

ABSTRACT

Maps of surface water fugacity of CO_2 (fCO_2) over eastern Fram Strait, south-western Nansen Basin, and the north-western Barents Sea (73–84°N, 5–46°E) from September 1997 to December 2020 were made and used to investigate seasonal and temporal trends. The mapping utilized a neural network technique, the self-organizing map (SOM), that was trained with different combinations of satellite/observational/model data of sea surface temperature (SST), sea surface salinity (SSS), mixed layer depth (MLD), chlorophyll *a* (Chl *a*), sea ice concentration, and atmospheric mole fraction of CO_2 (xCO_2). The trained SOM was labelled with available surface ocean fCO_2 data, and the labelled SOM was subsequently used to map the fCO_2. The produced maps reveal that fCO_2 in northern Barents Sea, at the border of the Nansen Basin, has increased significantly over the last decades by between 4.2 and 5.5 ± 0.6–1.1 µatm yr^{-1} over the winter to summer seasons. These rates are twice the rate of atmospheric CO_2 increase, which was about 2 µatm yr^{-1}. The spatial pattern coincides with the strongest decreases in sea ice concentration as well as with a salinification of the surface water. The former allows for a prolongation of the air-sea CO_2 flux with resultant oceanic CO_2 uptake in previously ice-covered waters, and the latter is caused by a shift from Arctic Water dominance to more saline waters containing more dissolved inorganic carbon, most likely of Atlantic Water origin although brine-release influenced deep water may also contribute.

1. Introduction

The eastern Fram Strait and the Barents Sea are the gateways for Atlantic Water (AW) that enters the central Arctic Ocean. Here, the warm AW meets the colder and fresher Arctic Water (ArW), as well as the sea ice, which results in a highly dynamic environment. As the oceanic heat content has increased, following the anthropogenic greenhouse gas induced climate change, the area has undergone remarkable changes (Ingvaldsen et al., 2021). The Barents Sea has warmed since the 1970s (e.g., Lind et al., 2018; Skagseth et al., 2020), which is linked to an increased inflow of warmer AW, and lost substantial sea ice cover (e.g., 50 % in annual sea ice cover between 1998 and 2008, Årthun et al., 2012; Smedsrud et al., 2022). At the same time, the water column stratification in the northern parts of the Barents Sea has weakened (Lind et al., 2018). This also coincides with alterations in the atmospheric forcing including an increased cyclone activity in the north-western Barents Sea (Wickström et al., 2019). The ongoing changes in the marine environment, that extend well into the Eurasian Basin of the Arctic Ocean, have been termed an "Atlantification" (Polyakov et al., 2017), and have been projected to expand further north in the coming years as the Barents Sea progresses to become sea-ice free (Årthun et al., 2019).

The current transitional state of the area affects air-sea heat and gas exchange, and consequently the capacity for CO_2 uptake from the atmosphere (Fransson et al., 2017; Graham et al., 2019). This highlights the need to track changes in the surface water fugacity of CO_2 (fCO_2) as

Abbreviations: fCO_2, fugacity of Carbon Dioxide; SOM, Self-Organizing Map; SST, Sea Surface temperature; SSS, Sea Surface Salinity; MLD, Mixed Layer Depth; Chl *a*, Chlorophyll *a*; xCO_2, Mole Fraction of Carbon Dioxide; AW, Atlantic Water; ArW, Arctic Water.

* Corresponding author.
E-mail address: ylva.ericson@npolar.no (Y. Ericson).

https://doi.org/10.1016/j.pocean.2023.103079

Available online 24 June 2023

well as to elucidate how the associated key drivers have changed over time and are likely to change in the future.

Several studies have focused on the spatiotemporal distribution of surface water fCO_2 and air-sea CO_2 fluxes in the Barents Sea (Omar et al., 2007; Lauvset et al., 2013; Yasunaka et al., 2018; Becker et al., 2021). Although underway surface water fCO_2 measurements on ships have increased the amount of data in the region, they are still quite sparse, in particular for the winter and early spring periods. To assess potential changes in fCO_2 in the area, it is consequently necessary to apply other methods. Satellite-, observational-, and model-based data products on sea ice concentration, sea surface temperature (SST), sea surface salinity (SSS), mixed layer depth (MLD), and chlorophyll *a* (Chl *a*), are growing in numbers as well as in quality. These products enable the use of algorithms, for instance based on multiple linear regressions (MLRs) or self-organizing maps (SOMs), to regionally map the surface water fCO_2 at a high spatiotemporal resolution (e.g., Lefévre et al., 2005; Telszewski et al., 2009; Lauvset et al., 2013; Yasunaka et al., 2016,2018). The quality of the produced fCO_2 maps depends on several factors including the spatiotemporal distribution of the fCO_2 measurements (Hauck et al., 2023), the chosen mapping method, and how representative the chosen satellite/observational/modelled data products are for the surface ocean's physical and chemical environment. There are several challenges here, first, the sea-ice cycle in the northern regions results in small-scale variability that many gridded satellite/observational/model products struggle to resolve. For instance, satellite SSS data have been available since 2009 but are limited to the open ocean and are sensitive to contamination at the sea-ice edge as well as the land–ocean margin (e.g., Xie et al., 2019; Supply et al., 2020). Secondly, the scarcity of fCO_2 measurements in sea-ice covered regions, especially back in time, limits the extent to which these methods can be constrained with real data. In fact, several studies have included sea ice concentration among the larger set of variables used to reconstruct the surface water fCO_2 for the region (e.g., Yasunaka et al., 2016,2018; Becker et al., 2021), despite lack of fCO_2 data in regions with high concentrations of sea ice (>70 %) before 2012. This is a weakness since the impact of sea ice on fCO_2 and air-ice-sea CO_2 exchange will depend on several factors including sea-ice type (i.e., multiyear and first-year ice), and stage in the annual sea-ice cycle (Rysgaard et al., 2011). The sea-ice composition in the Barents Sea used to be complex as it consisted of a mix of locally produced and imported sea ice of various ages (Vinje & Kvambekk, 1991), and the

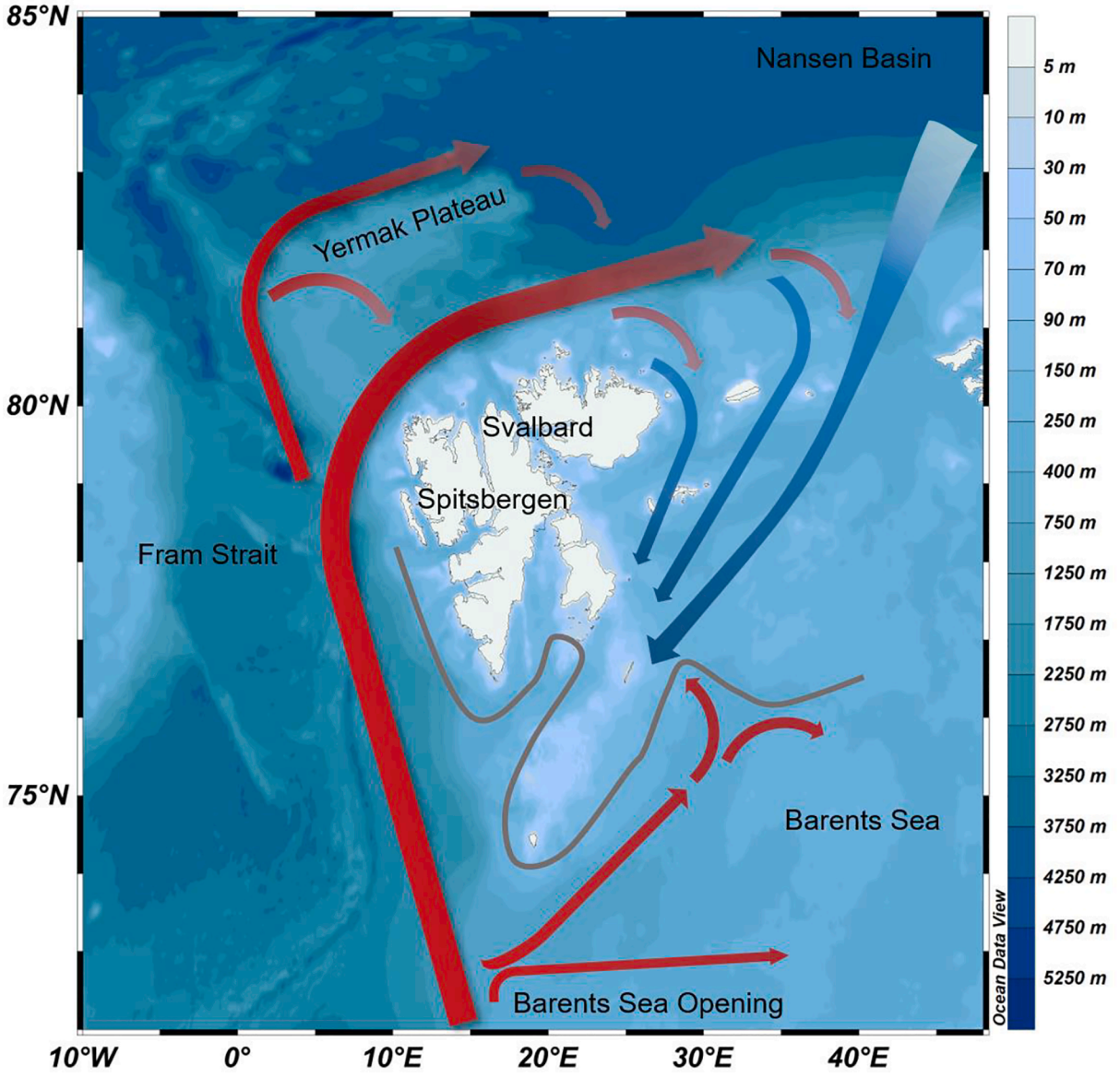

Fig. 1. Map over the study area including the currents of AW along the continental margin and over the Barents Sea Opening (red arrows). Blue arrows indicate the flow of ArW to the south. The grey solid line shows the Polar Front.

import of multiyear ice from the north could be quite variable (Kwok et al., 2005). However, the rapidly decreasing sea ice cover, especially in the Barents Sea (Årthun et al., 2012), together with a substantial decline in the multiyear ice in the Arctic Ocean in general (e.g., >50 % a decrease between 1999 and 2017, Kwok, 2018), show that sea-ice conditions in recent years are quite different from the conditions 20 years back in time.

Here we use observational, satellite, and model data in combination with surface ocean measurements of fCO_2 to investigate the utility of the SOM technique to map the surface water fCO_2 in the eastern Fram Strait, the south-western Nansen Basin, and the north-western Barents Sea region (Fig. 1). Seasonal maps of fCO_2 are created to evaluate the spatiotemporal variability, and drivers are discussed in a context of climate change.

2. Data and methods

2.1. In-situ data

This study is based on underway surface ocean fCO_2 measurements from SOCATv2021 (Surface Ocean CO2 Atlas, covering October 1999 to October 2020, for more details see Bakker et al., 2016), and from the R/Vs *Lance* (data from January to June 2015, Fransson et al., 2017) and *Kronprins Haakon* (measurements from August 2018 to December 2019). Measurements from the R/V *Kronprins Haakon*, were made by an autonomous instrument (General Oceanics® with a LI-7000 manufactured by LI-COR) using infrared analysis of headspace samples equilibrated with surface seawater (Fransson et al., 2023), with a setup and fCO_2 calculation following Pierrot et al. (2009). In addition, discrete measurements from several sources were used. These include data from the GLODAPv2.2021 data set (Lauvset et al., 2021) from between March 1998 and June 2019. Data from the years 2000, 2003 to 2005 from the carbon dioxide in the Atlantic Ocean (CARINA) data synthesis project (Key et al., 2010; Jutterström et al., 2010), and additional cruise data from between June 1999 and September 2019 (Chierici et al., 2019; Chierici & Fransson, 2019; Jones et al., 2021; Chierici et al., 2022). Data from the region 5°E <= longitude <= 46°E and 73°N <= latitude <= 84°N were used. The ranges were chosen to capture the area where the AW meets the ArW. The southern limit was chosen to avoid the freshening impact of the Norwegian/Murmansk Coastal Current that flows eastwards along the land margin of the Eurasian continent (see Fig. 1). The spatial distributions of the data sets are shown in Fig. 2a, b, and the temporal distribution in Fig. 2c.

The combined underway data set contains in total 458,516 fCO_2 measurements. After visual inspection a suspicious spike, consisting of four data points with no measurements directly before or after, was removed from the SOCAT data set (i.e., at 16:00 on 15 August 2017). All data sets included SST and SSS measurements, although the latter property is largely missing before 2005. For the SSS, suspicious data were removed for several cruises using either visual inspection (i.e., typically single points without measurements directly before or after) or three scaled median absolute deviations (MAD) away from the local median (window size of 6 h) to detect outliers. Also, note that SST data were not collected on the R/V *Kronprins Haakon* (KPH) in 2018. Instead, these were estimated from the equilibrator temperature using a mean temperature difference of 0.78 ± 0.2 °C (determined using KPH data collected in the same region in 2019). The uncertainty in the measured fCO_2 is around 5 µatm or better for the SOCAT data (Bakker et al., 2016) and KPH data. The R/V *Lance* data, which were largely collected in areas with sea ice, have a reported uncertainty of 7 µatm (Fransson et al., 2017).

The discrete water samples, 1141 measurements in total, were collected from Niskin bottles mounted on a rosette system including a conductivity, temperature, and depth (CTD) sensor package. Samples were analysed for total alkalinity (A_T) and total dissolved inorganic carbon (C_T), and in addition also for nutrients in most cases. Data were collected from the upper 15 m (depth < 16 m) to approximate the type of water that is sampled at the ship's sea water inlet, acknowledging that ship movement and especially the thrust can result in considerable mixing of the upper part of the water column. The A_T and C_T data were quality controlled for outliers using property-property plots with salinity as the independent variable. One point in A_T was removed (i.e., $S = 30.54$ and $A_T = 2201$ µmol kg^{-1}). The remaining A_T and C_T data, together with ancillary data of pressure, salinity, temperature, and if existent, phosphate and silicate concentrations were used to calculate the surface water fCO_2 using CO2SYS (van Heuven et al., 2011). When nutrient data were missing, they were assumed negligible in terms of their contribution to the total alkalinity (i.e., as suggested by the overall mean concentrations of 0.3 and 1.5 µmol kg^{-1} for phosphate and silicate, respectively). Moreover, the often-recommended constants for K_1 and K_2 of Mehrbach et al. (1973) as refitted by Dickson and Millero (1987) and the total borate formula of Lee et al. (2010) were used. Furthermore, the dissociation constant of bisulphate (K_{SO4}) of Dickson (1990) was used. The mean error of the calculated fCO_2 data was ± 11 µatm as estimated using the error function of Orr et al. (2018). This result is based on the following uncertainties of ± 4 µmol kg^{-1}, ±4 µmol kg^{-1}, ±0.01 °C and ± 0.05 in A_T, C_T, SST, and SSS, respectively. For phosphate and silicate, we used the standard deviation of 0.2 and

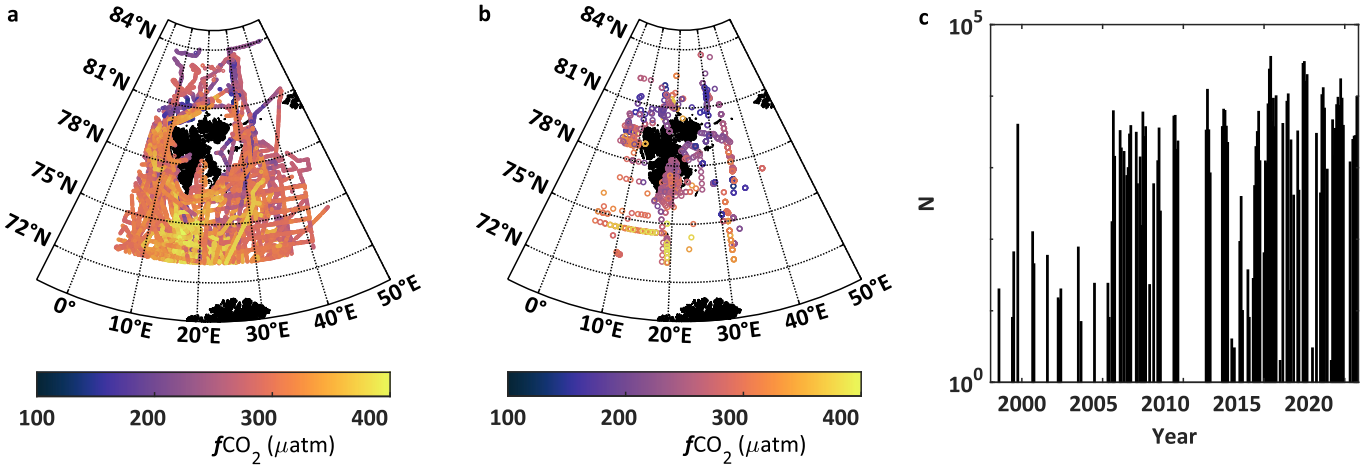

Fig. 2. (a) Underway surface water fCO_2 (µatm), (b) Calculated fCO_2 (µatm) from discrete samples, and **c)** Number of data points (N) per month between 1998 and 2020 (note the logarithmic scale).

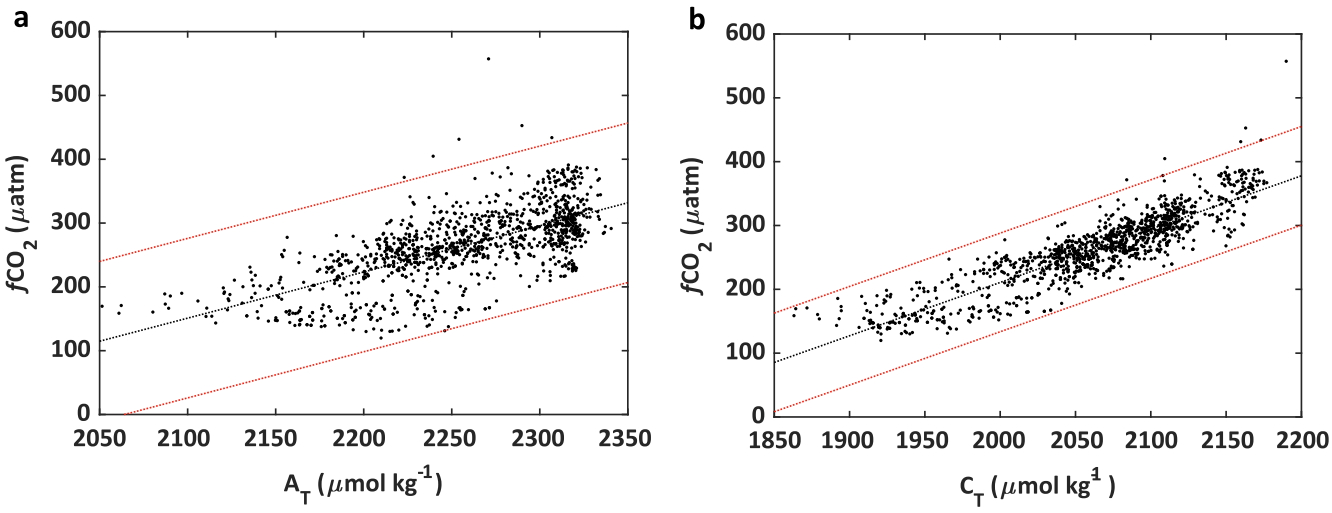

Fig. 3. Calculated surface water fCO_2 plotted against (a) discrete A_T measurements, (b) discrete C_T measurements. The red lines are 3 times the RMSE away from the fitted black line to show outlying fCO_2 data.

1.3 μmol kg^{-1}, respectively, as a measure of their uncertainties. We also used the default errors as suggested by Orr et al. (2018) for the total boron concentration and the dissociation constants. Finally, to sort out anomalous fCO_2 data, the calculated fCO_2 was plotted against A_T and C_T and data points with residuals>3 times the root mean square error (RMSE) of a robust fit (Fig. 3a, b) were considered outliers. In total 8 fCO_2 data points were thus removed.

2.2. Observational, satellite, reanalysis, and atmospheric xCO_2 data

Data products for SST, SSS, MLD, Chl *a*, sea ice concentration, and atmospheric mole fraction of CO_2 (xCO_2), were chosen based on their time span in conjunction with the time span of the underway data (Table 1). The SST, SSS, MLD, and Chl *a* data were obtained from Copernicus Marine Service (CMEMS). To facilitate the readability, we will refer to the SST from ESA SST CCI and C3S as ESA, SST, SSS, and MLD data from the Global Ocean Observation-based Product as MULTIOBS, and the SST, SSS, and MLD from the Arctic Ocean Physics Reanalysis product as TOPAZ, since the latter is based on the TOPAZ4 model.

Note that it has come to our knowledge that there are biased salinity profiles in January, with lower salinity than expected for the area at about 81-82°N and 5-7°E in the World Ocean Database, which affect the World Ocean Atlas 2018 (WOA18, James Reagan, personal communication). WOA18 is used as a first guess in the MULTOBS product and in the initialization of the TOPAZ4 model (note that the model is initialized in year 1991). This means that the two data products may be biased to fresher water in the wintertime in this area. To be transparent about the area that may be affected by the potential bias we include monthly mean maps of the SSS data for the years: 1998, 2001, 2010, and 2020 (see supplement, Figs. A1 and A2). In terms of the TOPAZ SSS, the bias affects the Nansen Basin in January, especially in the years before 2001. The impact of the bias is minor as the annual cycle progresses to March (Fig. A1). The MULTIOBS product is influenced by the low salinities in every January month (Fig. A2). Since these data are based on observations, the WOA18 bias has no influence on the other months.

In the present study the SSS data is used to train a neural network, and subsequently used to find matches between the network and a separate labelling data set, with associated fCO_2 measurements. These steps are based on the same SSS product and consequently we expect the

Table 1
Products used as training data.

	Data Product	Resolution	References
SST (°C)	ESA SST CCI (v2.0) and C3S Analyses	0.05° × 0.05°, daily	Good et al. (2019); Merchant et al. (2019)
	Global Ocean Observation-based Products, MULTIOBS_GLO_PHY_TSUV_3D_MYNRT_015_012	0.25° × 0.25°, weekly, monthly	https://doi.org/10.48670/moi-00052
	Arctic Ocean Physics Reanalysis, ARCTIC_MULTIYEAR_PHY_002_003	12.5 km × 12.5 km, daily, monthly	https://doi.org/10.48670/moi-00007
SSS	Global Ocean Observation-based Products, MULTIOBS_GLO_PHY_TSUV_3D_MYNRT_015_012	0.25° × 0.25°, weekly, monthly	https://doi.org/10.48670/moi-00052
	Arctic Ocean Physics Reanalysis, ARCTIC_MULTIYEAR_PHY_002_003	12.5 km × 12.5 km, daily, monthly	https://doi.org/10.48670/moi-00007
MLD (m)	Global Ocean Observation-based Products, MULTIOBS_GLO_PHY_TSUV_3D_MYNRT_015_012	0.25° × 0.25°, weekly, monthly	https://doi.org/10.48670/moi-00052
	Arctic Ocean Physics Reanalysis, ARCTIC_MULTIYEAR_PHY_002_003	12.5 km × 12.5 km, daily, monthly	https://doi.org/10.48670/moi-00007
Chl a (mg m^{-3})	Copernicus-GlobColour- reprocessed, OCEANCOLOUR_GLO_CHL_L4_REP_OBSERVATIONS_009_082	4 km × 4 km, interpolated daily	Garnesson et al., 2019
Sea ice concentration (%)	OSI-450 OSI SAF Global Sea Ice Concentration Climate Data Record/OSI-430-b OSI SAF Global Sea Ice Concentration Interim Climate Data Record	25 km × 25 km, daily	EUMETSAT Ocean and Sea Ice Satellite Application Facility (2017; 2019) Lavergne et al. (2019)
Atm. xCO2	Atmospheric Carbon Dioxide Dry Air Mole Fractions from the NOAA GML Carbon Cycle Cooperative Global Air Sampling Network	Close to weekly, monthly	Dlugokencky et al., (2021).

Table 2
Comparison between measured SST and SSS and corresponding satellite/observational/reanalysis data.

Properties	Mean Difference and STD	Linear Fit	Min. and max.
SST (°C)			
ESA SST at 0.2 m	−0.28 ± 0.83	1.01x + 0.27 $R^2 = 0.95$ RMSE = 0.83	−2.1, 10.8
MULTIOBS SST at 0 m	−0.17 ± 1.00	1.01x + 0.15 $R^2 = 0.92$ RMSE = 1.00	−3.0, 11.0
MULTIOBS SST at 10 m	−0.09 ± 0.90	1.00x + 0.08 $R^2 = 0.94$ RMSE = 0.90	−3.0, 10.3
TOPAZ SST at 0 m	−0.19 ± 0.87	1.00x + 0.19 $R^2 = 0.94$ RMSE = 0.87	−1.9, 10.3
SSS			
MULTIOBS SSS at 0 m	−0.16 ± 0.54	0.90x + 3.6 $R^2 = 0.50$ RMSE = 0.51	27.5, 35.4
MULTIOBS SSS at 10 m	−0.09 ± 0.50	0.95x + 1.7 $R^2 = 0.53$ RMSE = 0.49	27.5, 35.3
TOPAZ SSS at 0 m	0.07 ± 0.48	1.57x – 19.9 $R^2 = 0.41$ RMSE = 0.55	31.8, 35.1

Note: Min and max for the in-situ data were for SST −1.9 and 10.6 °C, respectively, and 29.0 and 35.3 for the SSS data.

impacts of the bias in WOA18 on the surface water fCO_2 estimation to be minor. Since the bias in the TOPAZ SSS is gradually diminishing, we also want to highlight that the labelling data set is sampled from the affected area in January 2014 and 2015, i.e., when the bias has a negligible impact on the SSS (Fig. A1). Still, winter fCO_2 estimates within this particular area should be interpreted with caution.

The Chl a data are from the Global Ocean Observation-based Products. These data were gridded all the way to 82.979°N. Please note, that due to light coverage, data are only available between April and September. To fill missing data between 82.979 and 84°N at each longitudinal grid line over the period with sufficient light, we set the Chl *a* concentration at 84°N to the minimum value observed between 82.5 and 83°N. This reflects that the sea ice concentration most often is higher further north and the resultant Chl *a* typically lower. Then we estimated concentrations between 82.979 and 84°N by using an interpolation of the form:

$$y = ae^{bx^{10}} \quad (1)$$

Where x is the numeric indices, with 1 at the 84°N latitude and increasing in the southward direction, and the a and b coefficients are given by the indices and Chl *a* concentrations at 82.979 and 84°N. This approach was chosen to reflect the rapidly declining Chl *a* concentration surrounding patches with higher algae biomasses, which will not be captured by a constant value or a linear approach.

Over the transitional phases (winter → spring/fall → winter) when the satellite coverage is gradually increasing or diminishing over approximately a month, we used a similar interpolation with the exponential function described above. This time, the value at 84°N was set to 0.025 mg m^{-3} and we interpolated values between the northernmost point with measurements and 84°N along each longitudinal grid line. Between October and March, data were missing due to the lack of sunlight. Since some productivity can take place under low light conditions (e.g., Randelhoff et al., 2020), we set the Chl *a* to 0.025 mg m^{-3}. This is the upper limit of concentrations observed by Randelhoff et al. (2018) west and north of Svalbard in January 2014. Low values between November and April in the northern Barents Sea are further supported by the findings of Henley et al. (2020), as well as by Fransson et al. (2017), i.e., low values in January throughout April, see Fig. 8a.

Unfortunately, for 1997 and 2020 the Chl *a* data were, for an unknown reason, not gridded all the way up north to 82.979°N. Both sea ice and cloud cover are factors that can explain this data sparsity. During the period with sufficient light nothing was done to fill the missing data. Over the remaining year we used the same procedures as described above.

Sea ice concentration data were obtained from the Ocean and Sea Ice Satellite Application Facility (OSI SAF), which is one of the centres of excellence within the European Organisation for the Exploitation of Meteorological Satellites (EUMETSAT). The mixing ratio of atmospheric CO_2 (xCO_2) was obtained from the Global Monitoring Laboratory (Dlugokencky et al., 2021). These bottle data were collected by the University of Stockholm at the Zeppelin Mountain, Ny Ålesund, Svalbard (Position: 78.907° N, 11.888° E, Station height: 474 m), with a near weekly or better resolution. Data flagged as bad, either with the rejected or selected flags (i.e., an alphanumeric other than a period (.)), were removed. Replicate samples were averaged, and outliers were detected using a moving median and a limit of three scaled median absolute deviations. The window size was half a year.

2.3. Comparison between SST and SSS from in-situ observations and satellite/observational/reanalysis data

Data from the different products were combined with the in-situ fCO_2 data using the nearest point in time and space. These data were compared against the measured in-situ SST and SSS data to identify the data product that fits the in-situ data best. The evaluation utilized the ranges of the different data sets, the mean difference including its associated standard deviation, and orthogonal linear regressions. The results are presented in Table 2. Please note that the in-situ data are given together with GPS latitude and longitude, which are

Table 3
Correlation coefficients, associated p-values and degrees of freedom (df) between trends in sea ice concentration in winter and significant trends in surface water fCO_2 in winter, spring, summer, and autumn.

Seasonal fCO_2 trends	Correlation coefficients	p-values	df
Winter	−0.55	0.000	7895
Spring	−0.63	0.000	7393
Summer	−0.06	0.000	8488
Autumn	0.23	0.000	8627

Table 4
Ranges of training data and SOM, their sizes, and percentage of label coverage, i.e., fraction in precent of training data and neurons that received fCO_2 labels.

Ranges Training Data	Size of training data	% labels	Ranges of SOM	Size of SOM	% labels
T SST: −1.9, 11.6 (99 %) T SSS: 29.2, 35.3 (100 %) T MLD: 2, 3500 (99 %) Chl *a*: 0.0, 42.3 (100 %) Sea ice: 0, 100 (100 %) Atm. xCO_2: 354, 421 (97 %)	6 × 10852683	43 %	SST: −1.9, 7.1 SSS: 33.1, 35.0 MLD: 7, 287 Chl *a*: 0.0, 0.4 Sea ice: 0, 93 Atm. xCO_2: 369, 411	162 × 102	33 %
E SST: −2.5, 12.0 (100 %) T SSS: 29.2, 35.3 (100 %) T MLD: 2, 3500 (99 %) Chl *a*: 0.0, 42.3 (100 %) Sea ice: 0, 100 (100 %) Atm. xCO_2: 354, 421 (97 %)	6 × 10849074	47 %	SST: −1.8, 7.1 SSS: 33.1, 35.0 MLD: 7, 273 Chl *a*: 0.0, 0.4 Sea ice: 0, 93 Atm. xCO_2: 369, 412	162 × 102	36 %
M SST: −3.0, 11.9 (100 %) M SSS: 27.2, 36.0 (100 %) M MLD: 10, 2814 (100 %) Chl *a*: 0.0, 42.3 (100 %) Sea ice: 0, 100 (100 %) Atm. xCO_2: 354, 421 (97 %)	6 × 10883383	48 %	SST: −1.7, 6.8 SSS: 31.4, 35.0 MLD: 14, 160 Chl *a*: 0.0, 0.5 Sea ice: 0, 94 Atm. xCO_2: 370,414	160 × 103	32 %
E SST: −2.5, 12.0 (100 %) M SSS: 27.2, 36.0 (100 %) M MLD: 10, 2814 (100 %) Chl *a*: 0.0, 42.3 (100 %) Sea ice: 0, 100 (100 %) Atm. xCO_2: 354, 421 (97 %)	6 × 10874857	50 %	SST: −1.8, 6.7 SSS: 31.4, 35.0 MLD: 14, 160 Chl *a*: 0.0, 0.5 Sea ice: 0, 95 Atm. xCO_2: 369, 414	160 × 103	36 %

georeferenced to the WGS84 datum and its associated ellipsoid. For most global observation/satellite-based products the given latitude and longitude grid is also based on the WGS84 datum. The TOPAZ-based reanalysis model product, on the other hand, is given with spherical coordinates on a polar stereographic projection. Consequently, it would seem most appropriate to do a datum shift before combining this data set with the in-situ data to avoid any latitudinal error (i.e., could be about 20 km in the mid-latitudes, Cao et al., 2017). However, the model, which utilize curvilinear coordinates, assimilates observational input without shifting the datum for the observational data (Jiping Xie, personal communication). Therefore, a datum shift could introduce more errors, and no shift was done in this study.

2.4. Self-organized map overview

The SOM technique was developed by Kohonen (2001) and allows for non-linear multidimensional relationships that do not require a priori knowledge on mechanistic relations. It has been used to map surface water fCO_2 over a wide range of spatial scales, i.e., coastal, regional, and global (Lefévre et al., 2005; Telszewski et al., 2009; Landschützer et al., 2013; Yasunaka et al., 2016,2018; Laruelle et al., 2017). The method has been thoroughly described by Telszewski et al. (2009), among others, and here we use a similar approach including the SOM Toolbox version 2.1 developed for Matlab 5, as used in their contribution (https://www.cis.hut.fi/projects/somtoolbox). In short, the SOM is a map of training data comprised of neurons that are, in this case, located on a regular flat map grid with a hexagonal lattice. The size of the map is given in Table 4 and was determined using the SOM Toolbox version 2.1 that calculates a sensible map size based on the training data. A smaller map size can increase the labelling success, but potentially at the cost of reduced data representation, i.e., important features may disappear. Each neuron has an associated prototype vector, in this instance, a unique combination of the six variables SST, SSS, MLD, Chl *a*, sea ice concentration, and atmospheric xCO_2. After a linear initialization, an iterative training process takes place, until neighbouring neurons have similar prototype vectors. A detailed description of this process can be found in Telszewski et al. (2009). A labelling data set, consisting of vectors of the six variables mentioned above, is subsequently used to find matches in the neural network. When a match is found that specific neuron will obtain a label, in this case a fCO_2 value. The labelled SOM can in turn be used to label the weekly fields that were used in the training process, and thus the surface water fCO_2 is mapped.

2.4.1. Training data

The training data used to precondition the SOM were weekly gridded fields of SSS, SST, MLD, Chl *a*, sea ice concentration, and xCO_2 at a 0.2°x0.2° resolution. Most data products were re-gridded and averaged to achieve this (see Table 1 for the spatiotemporal scales of the individual data sets). Note that the atmospheric xCO_2 data provided the network with time variability. These data were unfortunately missing for some weeks. A total of 1049 weeks of data between September 1997 and December 2020 were used, compared to 1218 weeks in total. This resulted in about 11 million vectors of the six variables, which should be sufficient to cover the regional variability in each of the variables. Both MLD and Chl *a* were logarithmically transformed because of skewness and all training data were normalized to obtain an even distribution before the actual training. This is important to minimize the influence of variables that have a large range of values on the map organization.

To test the performance of the different products outlined in Table 1 we created four different training data sets that resulted in four unique SOMs. We combined the Chl *a*, sea ice concentration, and xCO_2 data with, first, SST, SSS, and MLD from TOPAZ; second, SST from ESA, SSS and MLD from TOPAZ; third, SST at 10 m, SSS at 10 m, and MLD from MULTIOBS, and finally; SST from ESA, SSS at 10 m, and MLD from MULTIOBS. However, we only visualize the results using one of the SOMs, that is all produced fCO_2 maps, including temporal trends of

Table 5
SOM predictability using different training data, including coefficient of determination (R^2), RMSE, and Nash–Sutcliffe model efficiency index (ME, e.g., Stow et al., 2007).

Training data	Number of fCO_2 observations	R^2	RMSE (µatm)	ME
TOPAZ	459,644	0.77	23.2	0.76
Sea ice concentration = 0 %	332,070	0.77	18.8	0.76
Sea ice concentration > 0 %	127,574	0.62	31.6	0.57
Sea ice concentration > 70 %	99,727	0.68	27.4	0.65
TOPAZ with ESA SST	459,644	0.74	24.7	0.73
MULTIOBS	459,644	0.72	26.2	0.69
MULTIOBS with ESA SST	459,644	0.74	24.8	0.72

Note: Number of surface water fCO_2 observations were in total 459,644 in the comparisons between produced and observed data.

Table 6
SOM predictability using five subsets of test data, including R^2, RMSE, and ME.

Subset	Number of fCO_2 observations	R^2	RMSE (µatm)	ME
1	74,783	0.43	34.3	0.30
2	82,629	0.58	32.6	0.47
3	84,616	0.58	32.4	0.52
4	88,271	0.70	28.8	0.66
5	88,698	0.74	24.7	0.73
Average	**83,799**	**0.61**	**30.5**	**0.54**

fCO_2, that are presented below are based on the SOM that was trained with TOPAZ SST, SSS, and MLD.

2.4.2. Labelling data

When the training was completed, the neurons with their unique combinations of the six variables were, if possible, labelled with surface water fCO_2 data (rounded to integers). To achieve this, the surface water fCO_2 data (see Section 2.1) were combined with the six variables, sampled from the nearest point in time and space. We created four labelling data sets, using the same combinations of the data products described above in Section 2.4.1., although at their original spatiotemporal resolution (see Table 1). Note that the fCO_2 data used to label the SOM included only 26 discrete measurements in areas with high sea ice concentration (>70 %) prior to 2012. This can be compared to the 99,701 measurements obtained in such areas between 2012 and 2020. However, we included all data from March 1998 to October 2020, to utilize the efforts made to collect fCO_2 data.

Although all fCO_2 values were matched with neurons, only a third of the neurons received labels (see Table 4). This partly reflects the scarcity of fCO_2 data in high sea ice concentration areas back in time. When several values of fCO_2 were assigned to a specific neuron, the most common value (i.e., the mode) was used as a label. Note that it is important that the data used to label the neurons with the fCO_2 values cover close to the same ranges as the training data. This was achieved for each property with ≥ 97 % of the training data within the ranges of the labelling data set (Table 4).

Finally, the trained and labelled SOM was used to label the weekly gridded fields, which were next averaged to map the seasonal surface water fCO_2 (i.e., winter: December, January, February; spring: March, April, May; summer: June, July, August; autumn: September, October, November). This temporal averaging procedure increased the spatial coverage. The uncertainty in the computed averages is affected by the uncertainty in the individual fCO_2 estimates, which was approximated to 32 µatm by taking the root sum of squares of the algorithm RMSE and the fCO_2 measurement uncertainty, i.e., 30.5 µatm (see Table 6) and 11 µatm (see Section 2.1 under discrete measurements), respectively. This uncertainty is propagated in the averaging as follows:

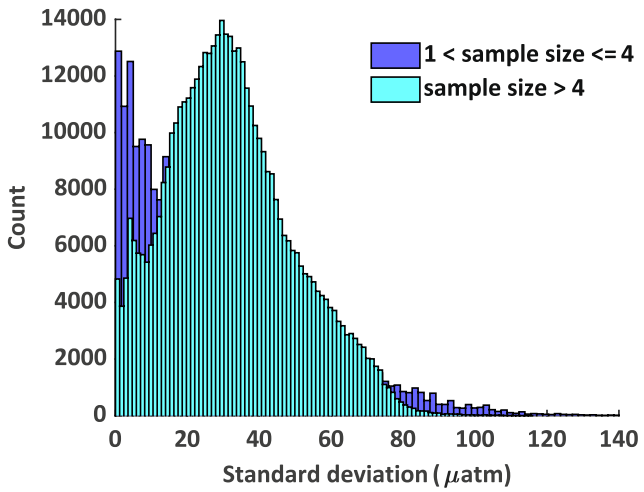

Fig. 4. Histogram of the standard deviation of the seasonal averages for sample sizes >1.

$$\Delta fCO_{2,\,\mathrm{mean}} = \frac{\sqrt{n\,32^2}}{n} \geq \frac{32\sqrt{14}}{14} = 9 \quad \mu\mathrm{atm} \tag{2}$$

where Δ refers to the uncertainty of the seasonal mean and n is the number of weekly estimates, which at most can be 14 weeks. Consequently, $\Delta fCO_{2,\mathrm{mean}}$ ranges between 9 and 32 µatm.

The lack of weekly fCO_2 estimates will also provide an additional source of uncertainty, especially when there is only one weekly estimate over the entire season. To answer how representative one value is for an entire season, the temporal variability must be considered as well. The lack of estimates reflects that there were few fCO_2 observations made historically at that specific time and combination of the six training variables. This lack does not necessarily mean that the temporal variability in the fCO_2 is larger than in a comparable season when there are many estimates. Consequently, under the assumption that periods with little data should have a comparable temporal variability, we can use the standard deviation presented in Fig. 4, which was centred around 30 µatm. Using the root sum of squares of 32 and 30 µatm, the seasonal averages based on only one weekly estimate are likely to have an uncertainty of about 44 µatm.

2.5. Calculation of air-sea fCO_2 gradient

The seasonal surface water fCO_2 maps in combination with the atmospheric xCO_2 data were used to calculate the air-sea fCO_2 gradient (i.e., the difference between the mapped surface water fCO_2 and the atmospheric fCO_2). The atmospheric xCO_2 data were averaged over seasons and subsequently converted to fCO_2 according to Pierrot et al. (2009) and references therein e.g., Weiss (1974).

3. Results

3.1. Seasonal surface water fCO_2 maps

Fig. 5 shows the seasonal maps for three selected years, 2000, 2010, and 2020. Especially the winter maps have grid points that lack labels, although this is largely year dependent. Still, it is possible to distinguish some important features in the area. In general, the surface water fCO_2 is higher in the AW influenced south-western part of the investigated area than in the ArW influenced parts in the north. The intrusion of AW across the Barents Sea Opening and into the southern parts of the Barents Sea is quite visible in all seasons (e.g., Fig. 5l). North of the Yermak Plateau, as well as north and northeast of Spitsbergen, surface water with lower fCO_2 is apparent. There is also a strong seasonal signal with generally

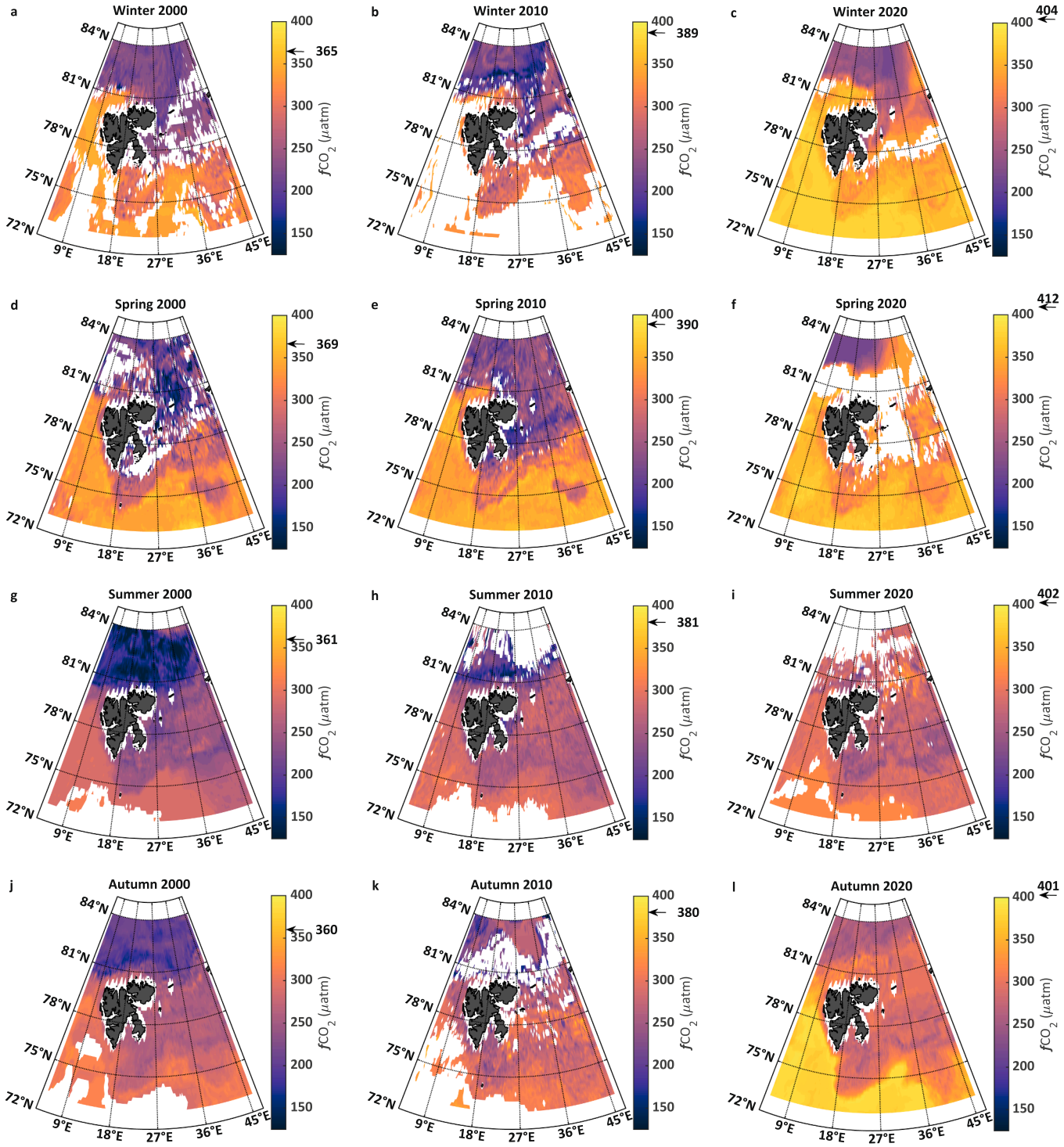

Fig. 5. Estimated fCO_2 in (a) winter 2000, (b) winter 2010, (c) winter 2020, (d) spring 2000, (e) spring 2010, (f) spring 2020, (g) summer 2000, (h) summer 2010, (i) summer 2020, (j) autumn 2000, (k) autumn 2010, (l) autumn 2020. The arrows next to the colour bars point to the atmospheric fCO_2 value for the specific years and seasons.

lower fCO_2 values in summer than in winter. Regardless, the surface water fCO_2 is largely undersaturated with respect to the atmosphere in all seasons, i.e., only 0.04 % of the labelled data are equal to or higher than the atmospheric fCO_2 (in total 336 data points essentially all from the winter and spring seasons). The difference between the surface water and atmospheric fCO_2 ranges between −270 and 24 µatm. These are also the ranges during the spring season, which shows the largest variability. Apart from this, a noticeable interannual change is observed in the surface water fCO_2 in all seasons, with increasing fCO_2 in recent years. This feature will be further investigated in the sections below.

3.2. *Trends in seasonal surface water fCO_2*

To assess the potential changes in the seasonal surface water fCO_2, we calculated temporal trends in all grid points with at least 15 estimated seasonal values in the period between September 1997 and

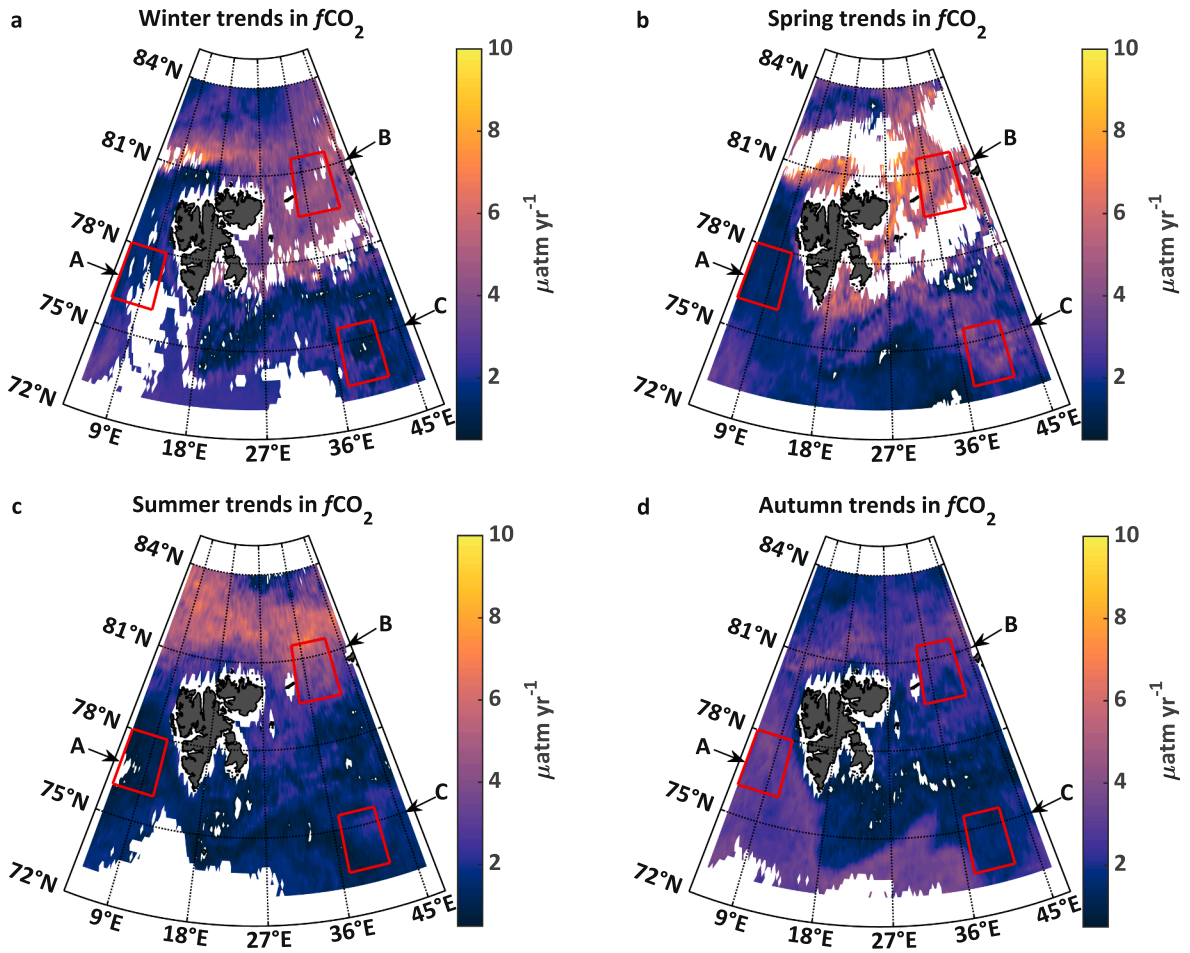

Fig. 6. Trends in surface water fCO_2 in (a) winter, (b) spring, (c) summer, and (d) autumn. The selected localities A, B, and C are specificed by the red boxes.

December 2020 (99 % of these trends extended from 2000 and earlier to 2019 and later). To account for the uncertainty in the seasonally averaged fCO_2 we also applied a simple Monte Carlo approach. Normally distributed artificial random errors (n = 1000) with a mean of zero and a standard deviation of 44 µatm (see Section 2.4.2) were added to the seasonal averages and a thousand linear regressions were performed at each grid point. The standard deviation of these trend estimates was then used as a measure of the uncertainty, on average 1.4 ± 0.1 µatm yr^{-1}.

The fCO_2 trends presented below are mostly significant (p values < 0.05, Figs. B1a-d). Spots with insignifcant trends are also scattered over the study area, especially in the area over which the Polar Front fluctuates. This is the area where the AW meets the ArW in the Barents Sea (Fig. 1), such that interannual variability may obfuscate any trend over the time period considered. The signficant fCO_2 trends are always positive (increasing fCO_2). To highligth the regional variability we selected three localites where we spatially averaged the significant trends, i.e., an AW-influenced site (box A in Fig. 6a-d), a sea-ice influenced site (box B in Fig. 6a-d), and a south-eastern Barents Sea site (box C in Fig. 6a-d). Note that as the uncertainity of the individual trends (i.e., around 1.4 µatm yr^{-1}) is propagated in the average calculations, the combined uncertainty becomes 0.1 µatm yr^{-1} or less (i.e., the sample sizes ranged between 228 and 397). Also, note that missing values can largely be filled with a lower limit for the linear regressions (e.g., setting the limit to 11 estimated seasonal values), this will not change the calculated averages.

In the western locality with AW the significant trends are on average 1.7 ± 0.3, 1.4 ± 0.2, 1.0 ± 0.2 and 3.1 ± 0.4 µatm yr^{-1}, in winter, spring, summer, and autumn, respectively. In the sea-ice influenced north-eastern site, the corresponding increase rates are 4.2 ± 0.6, 5.5 ± 1.1, 4.2 ± 1.0, and 2.6 ± 0.4 µatm yr^{-1}, in winter, spring, summer, and autumn, respectively. Finally in box C the spatially-averaged significant trends are 1.8 ± 0.6, 3.0 ± 0.8, 1.5 ± 0.5, and 1.6 ± 0.3 µatm yr^{-1}, in winter, spring, summer, and autumn, respectively. Note that the standard deviations given here represent the regional variability in the trends. It is clear that the strongest trends occur in the northern and north-eastern parts of the region, which are influenced by the sea-ice cycle and dominated by ArW with lower salinity due to sea-ice melt. This is in particular the case for the winter, spring and summer seasons. In autumn the trends are much more comparable across the entire study area.

3.3. Trends in drivers

The seasonal trends in the atmospheric fCO_2 are 2.1, 2.2, 2.2, and 2.1 µatm yr^{-1} in winter, spring, summer, and autumn, respectively. Since the atmospheric xCO_2 is spatially homogenous in the training data, these trends cannot explain the spatial distribution of the trends in the surface water fCO_2. Fig. 7a-d show trends in the sea ice concentration. Here, only negative trends are significant (Figs. B2a-d). The mean sea-ice concentration decreases with significant trends at -1.7 ± 0.7, -1.0 ± 0.6, -0.8 ± 0.4, and -1.3 ± 0.7 % yr^{-1}, in winter, spring, summer, and autumn, respectively. The standard deviations presented here reflect the spatial variability in the sea ice loss. In the AW influenced box A there are significantly decreasing trends in spring of on average -0.3 ± 0.2 % yr^{-1} close to the continental shelf (Fig. 7b). In the northern Barents Sea, i.e., in box B, the sea ice disappears at a rate of on average -1.7 ± 0.2, -0.8 ± 0.2, and -2.3 ± 0.3 % yr^{-1} in winter, spring, and

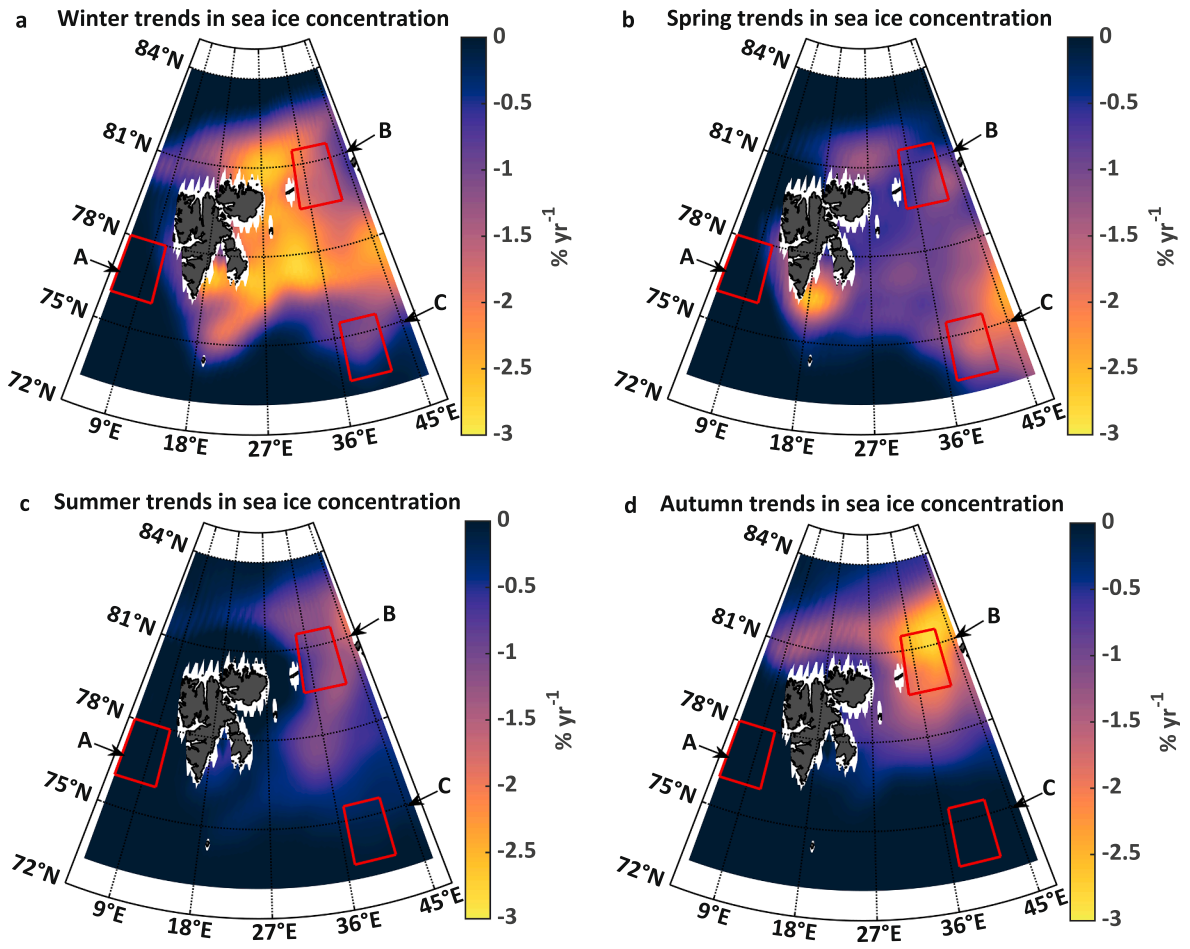

Fig. 7. Trends in sea ice concentration in (a) winter, (b) spring, (c) summer, and (d) autumn.

autumn, respectively. In summer the trends are insignificant, which likely reflect large interannual variability. In the eastern box C, significant sea ice losses of on average -0.7 ± 0.3, -1.4 ± 0.4, -0.3 ± 0.0 % yr^{-1} are observed in winter, spring, and summer, respectively.

The decreases in sea ice coincide with strong trends in the surface water fCO_2. However, there appears to be a seasonal lag in the latter in such a way that the changes in sea ice in autumn show a similar distribution as the largest changes estimated in the surface water fCO_2 in winter. The same feature is also observed in the winter sea-ice distribution compared to changes seen in fCO_2 in spring. To illustrate this, we show correlations between the trends in winter sea ice concentration and significant trends in surface water fCO_2 (Table 3). Note that the sea-ice reduction observed in spring and summer do not coincide with especially strong trends in the surface water fCO_2 in summer and autumn.

Null hypothesis is that there is no correlation between the trends in the winter sea ice concentration and the seasonal surface water fCO_2 trends (alpha is set to 0.05).

Fig. 8 shows that there is a trend of increasing salinity in the northern Barents Sea and Nansen Basin area. Especially strong trends occur in winter in the Nansen Basin, north of Spitsbergen. These trends should be interpreted with caution in the light of the biased salinity in WOA18 in the area of 81-82°N and 5-7°E that affects the TOPAZ4 model. Apart from these, the positive trends most likely reflect an increased influence of AW, which has a higher fCO_2 compared to ArW as shown in Fig. 5. This signal of Atlantification can result from increased inflow of AW to the area, loss of sea-ice melt water on top of the AW, and/or vertical mixing. Increased vertical mixing may also bring C_T (e.g. CO_2) rich deep water impacted by brine release to the surface. The strong salinity trends are in general significant (p values < 0.05, see Appendices Figs. B3a-d), with mean salinity increases of 0.02 ± 0.01, 0.01 ± 0.01, 0.01 ± 0.01, and 0.01 ± 0.01 yr^{-1} in winter, spring, summer, and autumn, respectively.

In the western box, A, the SSS is increasing significantly in the northern part in spring and summer, although at an order of magnitude lower rates than the average trends presented above. In box B, salinity increases significantly by 0.01 ± 0.00 yr^{-1} in parts of the area throughout the year. In box C, there are also patches with significant trends in all seasons, but as in box A at very low rates.

Note that it is not the change in salinity in itself that results in a significant change in fCO_2, i.e., a change in salinity of 0.01 yr^{-1}, will only have a minor impact on the solubility of CO_2 and consequently on the surface water fCO_2. It is most likely the shift from a less saline water mass with lower fCO_2 to a more saline water mass with higher fCO_2 that impact the surface water fCO_2.

Changes in the MLD will affect the chemical compostion of the surface water (e.g., a deepning can reflect increased mixing with subsurface layers and a shallowing can reflect sea ice melt water) and have a direct impact on the time scale for air-sea equilibrium, which is important for the surface water fCO_2 evolution. Such changes should also be reflected in the TOPAZ MLD data. There are both positive and negative significant trends, i.e., deepening and shoaling of the MLD, respectively (Fig. 9a-d, Figs. B4a-d). For instance, in winter, spring, and autumn there has been a significant deepening of the MLD over the years, especially east of Spitsbergen (Fig. 9a, b, d). This distribution agrees to some extent with the area where the sea ice concentration has decreased (Fig. 7). In summer, there is a deepening of the MLD south of approximately 81°N, except for in an area east of Bear Island (Fig. 9c). The mean values of the

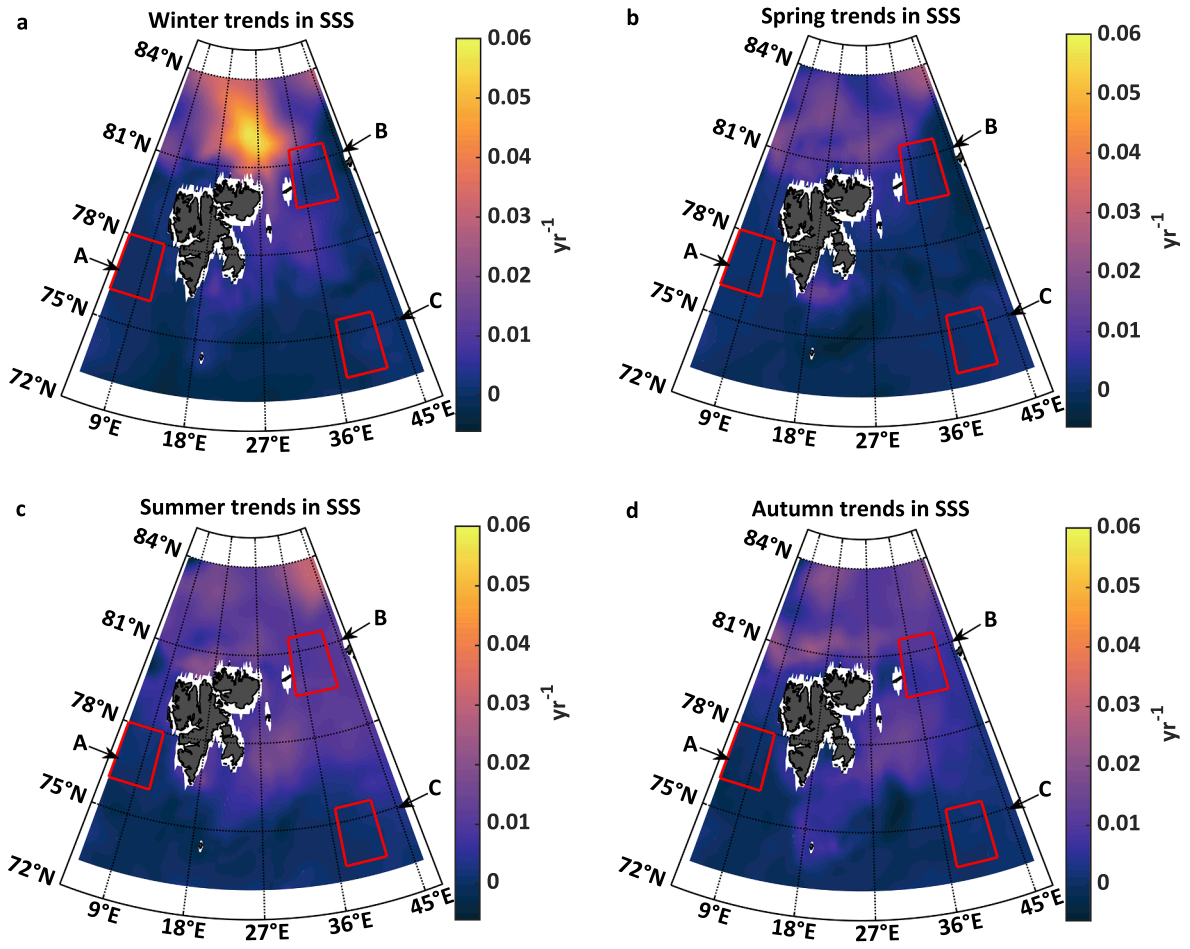

Fig. 8. Trends in SSS in (a) winter, (b) spring, (c) summer, and (d) autumn. Note that this is the modelled reanalysis data from TOPAZ.

significiantly increasing trends and their spatial standard deviation are 1.1 ± 1.3, 1.9 ± 2.9, 0.3 ± 0.1, and 0.5 ± 0.2 m yr^{-1} in winter, spring, summer, and autumn, respectively (Fig. 9a-d). The deepning is visible in the northern box B, with significant trends of on average 0.9 ± 0.1, 0.5 ± 0.1, 0.4 ± 0.1, and 0.6 ± 0.1 m yr^{-1} in winter, spring, summer, and autumn, respectively. In the eastern box C, there is a significant deepening in the north-eastern corner of on average 1.4 ± 0.2 and 2.1 ± 0.6 m yr^{-1} in winter and spring. In summer, the deepening is widespread but much weaker, with an average of 0.2 ± 0.0 m yr^{-1}. In summer, the deepening is also present in the AW influenced box A, with a weak average rate of 0.2 ± 0.0 m yr^{-1}.

These positive trends could contribute to the estimated strong trends in the surface water fCO_2 in the area, i.e., if the freshwater layer on top of the AW has dissappeared following the decline in sea ice or if deep water with higher C_T content is brought to the surface. The changes in MLD show similarities to those of SSS, but do not extend as far into the Nansen Basin (Fig. 8). This suggests that the trends in SSS not only result from increased mixing, but also result from a larger dominance of AW. Especially west of the continental margin of Spitsbergen there is a significant shoaling of the MLD in winter and spring. The averages of the decreasing MLD trends for these two seasons are -5.7 ± 4.5 and -6.1 ± 4.9 m yr^{-1} in winter and spring, respectively. This shoaling is also apparent in box A, with significant decrease rates of on average -9.9 ± 2.9 and -8.8 ± 2.0 in winter and spring, respectively.

Water column stratification is also dependent on the ocean heat content. The SST, which has a direct thermodynamic impact on the surface water fCO_2, will also indicate changes in the ocean heat balance.

In the figures below, trends in SST from ESA are shown (Fig. 10a-d). This data set, which is based on satellite measurements, was chosen as it reflects the actual surface layer the best, see below. The trends, if significant, are positive, especially along the western and southern parts of Svalbard, but also in the south-eastern area where box C is located (Figs. B5a-d).

In the western box A, signficant trends of on average 0.05–0.06 $\pm$ 0.01–0.02 °C yr^{-1} are observed, except for the summer season. In this particular season there is a patch with significant trends at the northern border of on average 0.03 ± 0.01 °C yr^{-1}. These rates can be compared to the significant but largely weaker trends in the northern box B of on average 0.01 ± 0.00, 0.04 ± 0.01, and 0.03 ± 0.01 °C yr^{-1} in winter, summer, and autumn, respectively. In spring the significant trends are an order of magnitude lower. In the eastern box C stronger mean trends are observed of between 0.06 and 0.07 ± 0.01 °C yr^{-1}, although there were no signficant trends in the summer season.

In general, the significant trends do not follow the pattern seen in SSS and MLD in winter and spring. The summer season differs slightly, since the trends mostly are insignificant south of 81°N (Appendix Fig. B5c). In autumn there are similar features in the distribution of strong trends compared to that of SSS (Fig. 10d, Fig. 8d). Regardless, the distribution of the significant trends in SST cannot explain the strong trends in the surface water fCO_2, but they contribute to the increases in fCO_2 where they are positive. The mean values of the significant trends over the entire study area are 0.04 ± 0.03, 0.04 ± 0.04, 0.02 ± 0.02, and 0.04 ± 0.02 °C yr^{-1}, in winter, spring, summer, and autumn, respectively. This will increase the surface water fCO_2 with about 0.5 µatm yr^{-1} (i.e., using the fCO_2 and temperature relation by Takahashi et al., 1993). In areas where the temperature trends are especially strong, the change will be>1 µatm yr^{-1}.

Because of the lack of light, satellite data cannot be used to detect

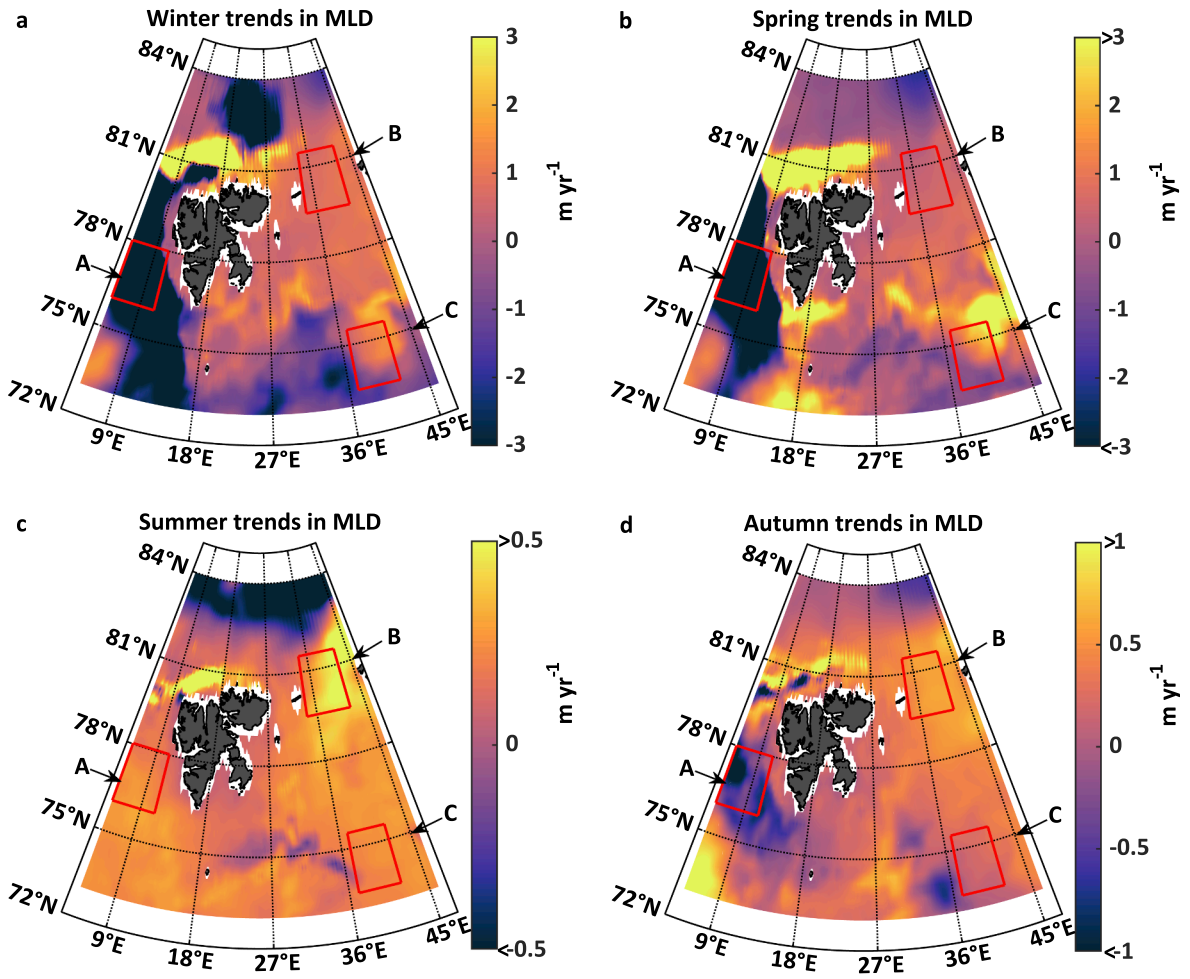

Fig. 9. Trends in MLD in (a) winter, (b) spring, (c) summer, and (d) autumn. Note the different scales on the colorbars. Also, note that this is the modelled reanalysis data from TOPAZ.

changes in primary production over the winter season (i.e., December to February). Consequently, the spatial homogenous wintertime Chl *a* that is set to 0.025 mg m^{-3} cannot explain the spatial distribution of the trends in the surface water fCO_2 in winter. In spring, there is a patch of significantly decreasing trends in Chl *a* west of Spitsbergen close to the continental slope (Fig. 11a, Fig. B6a). These are present in box A with an average decrease rate of -0.01 ± 0.01 mg m^3 yr^{-1}. In the north-western corner of the Nansen Basin there are also significantly decreasing trends, although closer to zero. This feature is also observed in summer and autumn (Fig. 11b-c, Fig. B6b-c). In summer there are patches with significantly increasing trends west of Spitsbergen. The average incresase rate in box A is 0.01 ± 0.00 mg m^3 yr^{-1}. In autumn, there is a patch with positive trends close to the north-western tip of Spitsbergen. In general, all significant trends are weak and the resultant changes in Chl *a* over two decades are less than ± 1 mg m^3.

3.4. SOM performance

The most successful combinations to label the neurons are the SST from the ESA in combination with either the SSS and MLD from TOPAZ or the correspondent properties at 10 m from MULTIOBS, i.e., 36 % of the neurons are labelled (Table 4). Apart from an offset of -0.28 °C, the ESA SST also agrees best with the measured SST (see Table 2). The SST from the TOPAZ or MULTIOBS gives fewer labelled neurons, 33 % and 32 %, respectively. The subsequent labelling of the weekly grids is most successful using MULTIOBS, either with the included SST or in combination with the ESA SST, i.e., 48 and 50 % of the training data are labelled, respectively. The corresponding values for TOPAZ using either the TOPAZ or ESA SST are 43 and 47 %, respectively.

Note: The training data extends between September 1997 and December 2020. Abbreviations stand for: T = TOPAZ, E = ESA, and M = MULTIOBS. Within brackets are the percent of the training data that are within ranges of the labelling data set.

In terms of skill assessment, as revealed by comparisons between estimated and observed surface water fCO_2 data, the TOPAZ product performs better than the MULTIOBS product, i.e., higher R^2, ME, and lower RMSE (Table 5). This supports the use of TOPAZ over the MULTIOBS product in future studies. The labelling success will be slightly improved if the TOPAZ data is used with the SST of ESA, although the model performance is better with the TOPAZ SST. Note that this only reflects how well the different products combine to estimate fCO_2 and not how accurate the products are in themselves. Based on this model performance result, all figures with produced fCO_2 data, as stated in Section 2.4, show results from the training data that included the TOPAZ data. Fig. 12a and c show histograms of the differences between estimated and observed fCO_2 data prior to 2010 and from 2010 and onwards. These differences are centred around zero and their distribution (Fig. 12b, d) shows no spatial patterns, although large differences are found in the area close to the continental margin and land, especially for the earlier period. It is also clear that the R^2 and ME are considerably lower and RMSE higher in ice-covered waters compared to open waters (Table 5). The method performs worse in ice-covered waters where the concentration is<70 %. This may reflect the uncertainty that results from pairing fCO_2 measurements with satellite sea ice concentration

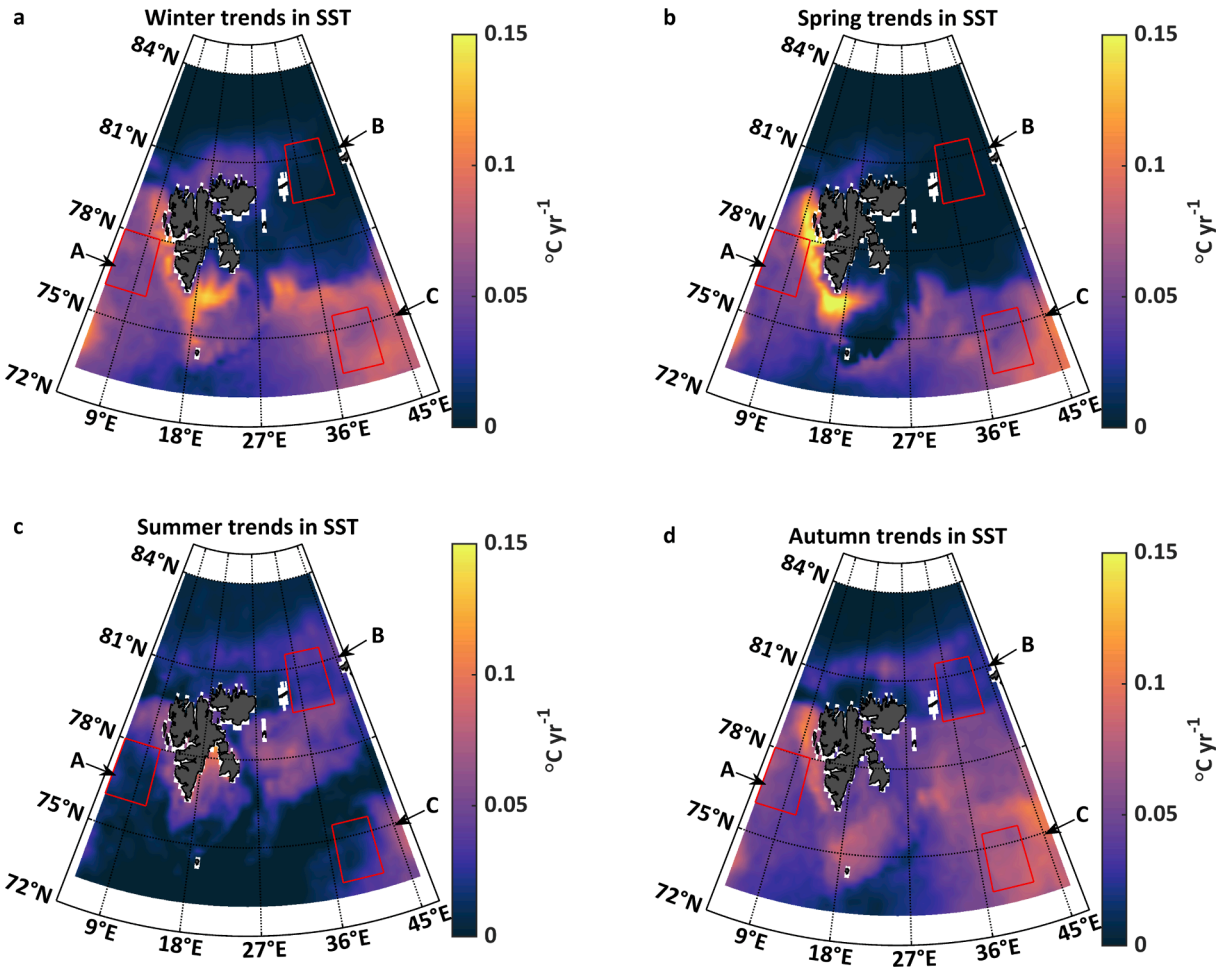

Fig. 10. Trends in SST in (a) winter, (b) spring, (c) summer, and (d) autumn. Note that this is the SST from ESA.

data based on the nearest point in time and space. When the sea ice concentration is low the possibility to erroneously combine fCO_2 measurements in open waters with ice-covered waters, or the opposite, is larger. Low sea ice concentrations also relate to processes such as melting and freezing that can result in highly variable fCO_2 values due to several physical- and biogeochemical processes.

As a final test of the model performance, we used a K-fold cross-validation. This is a data efficient approach, which is preferable considering the scarcity of fCO_2 observations historically. This also allows for testing the SOM on data with a more comprehensive representation of the spatiotemporal distribution in the fCO_2. We divided the labelling data set into five equally sized subsets. These were created by combining segments of 1000 and 50 measurements from the underway and discrete measurements, respectively. Note that 50 measurements of discrete surface fCO_2 typically reflects data from several cruises. In terms of 1000 measurements, these can also be from an individual cruise data set, but larger data sets will be divided among several subsets. In the cross-validation procedure we used one of the subsets as a test set and labelled the SOM with the remaining subsets. The labelled SOM was then used to label the test set and the model performance was evaluated. We repeated this process, each time using another subset as the test set. The results from the test steps are presented in Table 6. The average ME of 0.54 can be regarded as a good performance (0.5–0.65, Marechal, 2004), but is lower than the estimated ME for the entire labelling data set of 0.76 (Table 5), which corresponds to a very good performance ($0.65 < ME < 0.85$, Marchel, 2004). The average R^2 and RMSE are 0.61 and 30.5 µatm, respectively, which can be compared to 0.77 and 23.2 µatm, respectively, for the entire labelling data set. Note that the mean RMSE of 30.5 µatm can be considered as an approximation of the uncertainty in the fCO_2 estimates using the SOM algorithm. Of course, the uncertainty in the estimated fCO_2 will also depend on the uncertainty in the observed fCO_2, which is about 11 µatm or better depending on the data source.

Note: The different sizes of the subsets depend on lack of labels in the labelling process of the test data.

4. Discussion

4.1. Spatiotemporal distribution in fCO_2

In the present study we found especially strong trends in sea surface fCO_2 of 4.2–5.5 ± 0.6–1.1 µatm yr^{-1} on average, in winter, spring, and summer in the northern Barents Sea at the southern border of the Nansen Basin (i.e., box B in Fig. 6a-c, approximately for the period 2000 to 2020). Apart from the autumn season, with an average trend of 2.6 ± 0.4 µatm yr^{-1}, these trends are twice as high as the atmospheric increase rate in fCO_2 of about 2 µatm (Dlugokencky et al., 2021). This means that the oceanic capacity for CO_2 uptake on average has decreased. Such strong trends have not been observed in this part of the Arctic Ocean before. For instance, Becker et al. (2021) estimated insignificant trends in this north-eastern corner between 1998 and 2016. Over the remaining Barents Sea they estimated trends from 0.5 to 1.5 µatm yr^{-1}, which are on the lower side of the trends we estimated for the middle of the Barents Sea (i.e., 1.5–3.0 ± 0.3–0.8 µatm yr^{-1}). On the Atlantic side of the study area the spatially averaged trends ranged between 1.0 and 3.1 ± 0.2–0.4 µatm yr^{-1}, with the highest rate observed in autumn. These trends are

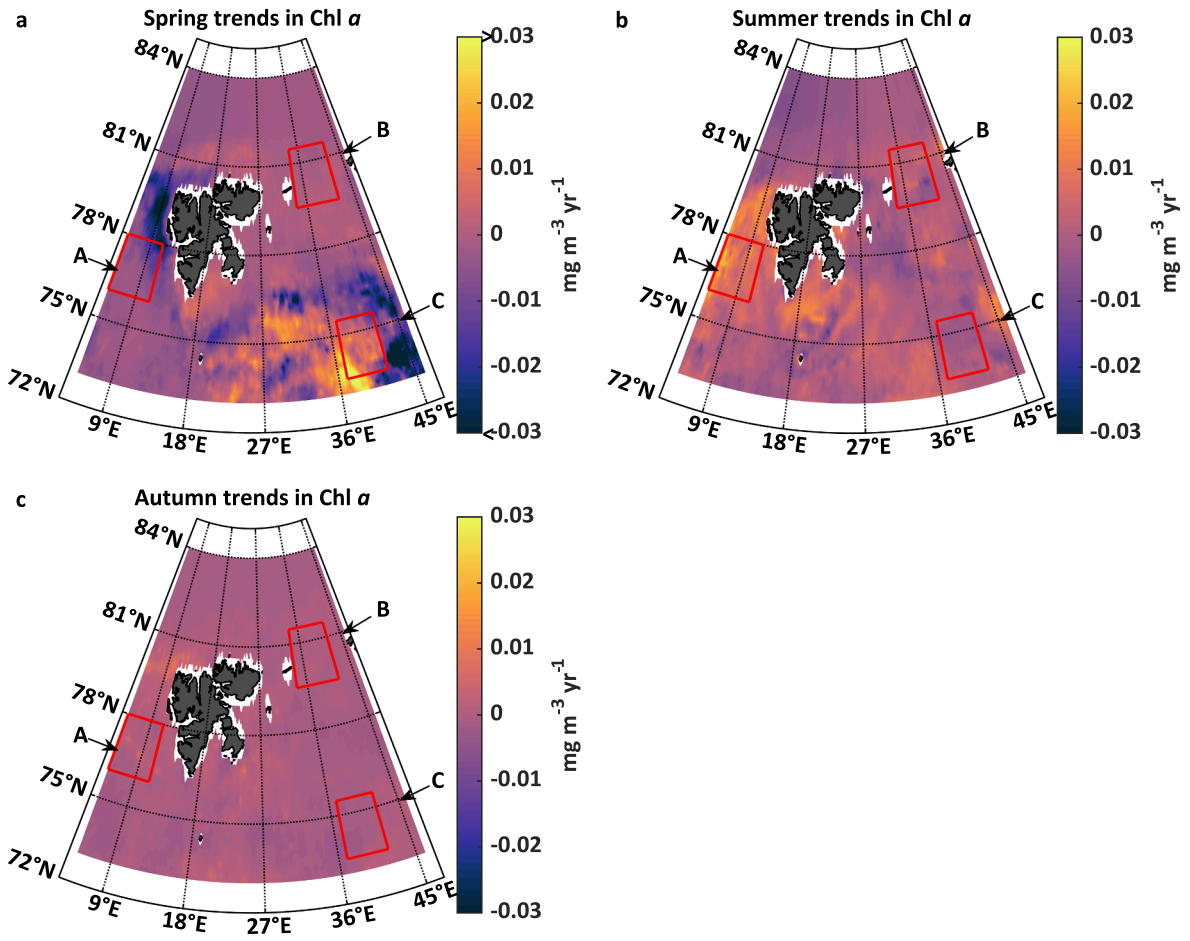

Fig. 11. Trends in Chl *a* in (a) spring, (b) summer, and, (c) autumn.

more comparable to the atmospheric fCO_2 rise as well as of oceanic trends estimated in AW further south (2.9 µatm yr^{-1}, Ocean Weather Station M in the Norwegian sea, Skjelvan et al., 2022), and in AW in the Barents Sea Opening and in the Fram Strait (1.5 and 1.9 µatm yr^{-1}, respectively, Fransner et al., 2022, see Table S11). Note that neither of the mean trends in the present study are calculated in the area where we see the strong trends in salinity in winter, that may be affected by the bias in WOA18 (Fig. 8a).

The northern Barents Sea and southern Nansen Basin are areas largely influenced by the seasonal sea-ice cycle and data are especially sparse there. Therefore, it is interesting that Becker at al. (2021) determined insignificant trends there. Insignificant trends can reflect large interannual variability in the estimated surface water fCO_2, little interannual variability with no temporal change, or a non-linear evolution of the surface water fCO_2. Regardless, the temporal evolution of the fCO_2 estimated in the present study in this specific area must differ from the fCO_2 produced with the methods of Becker et al. (2021). This illustrates the sensitivity of our different methodologies to the lack of data. Becker et al. (2021) hypothesized that the low trends in the Barents Sea resulted from an earlier onset of the phytoplankton bloom, in particular in the north where sea ice is disappearing, with the potential of a longer growth season. A longer growth season may imply higher concentrations of Chl *a* over a longer period, however, there were no significant trends in the seasonal Chl *a* in the parts of the Barents Sea that were included in the present study (Fig. 11a-c, B6a-c). Lewis et al. (2020) on the other hand did show that Chl *a* in the Barents Sea increased significantly by 0.02 mg m^{-3} yr^{-1} between 1998 and 2018, with the strongest trends in the middle of the Barents Sea. This agrees with the strongest, although insignificant, increasing spring trends that were estimated in Chl *a* in the present study (Fig. 11a, Fig. B6a). The production of this organic material is likely to have a seasonally dampening impact on the rise in surface water fCO_2 and may also have an annual impact if the carbon is exported to the sediments. In the present study in summer and autumn, weaker and even insignificant trends were found south of 79°N in the Barents Sea (Fig. 6c-d).

We argue that there are several causes for the strong trends in fCO_2 observed in the present study. First, the anthropogenic increase in atmospheric CO_2 will add to an increase in C_T in the surface ocean. This has been estimated to be about 0.2 and 0.8 µmol kg^{-1} yr^{-1} in the Barents Sea Opening and the Fram Strait, respectively (Fransner et al., 2022, only the latter is significant). For a water mass with a winter C_T around 2160 µmol kg^{-1} yr^{-1} and a Revelle Factor around 14 (i.e., typical for transformed AW in the West Spitsbergen area, Ericson et al., 2019), the latter change corresponds to an increase in fCO_2 of about 2 µatm or less depending on the surface water fCO_2 (e.g., $fCO_2 < 400$ µatm). Second, the sea ice concentration has decreased considerably, especially in the northern parts, which allows the air-sea CO_2 gradient to become closer to equilibrium with the atmosphere in recent years compared to 20 years back in time. It has been shown that sea ice loss in the Canada Basin amplifies the increase in the surface water fCO_2 (Ouyang et al., 2020; Qi et al., 2022), with an estimated trend of 4.6 µatm yr^{-1} between 1994 and 2018 (Ouyang et al., 2020). The importance of sea ice on the surface water fCO_2 increase rate has also been noted by Smedsrud et al. (2022) that estimated that the oceanic uptake of CO_2 had increased substantially in the Barents Sea due to loss of sea ice. At the same time, there has been noted more wind activity in the northern parts of the study area (Wickström et al., 2019), which will increase the air-sea CO_2 flux as well as the ocean mixing. Increased mixing in the northern part of the Barents

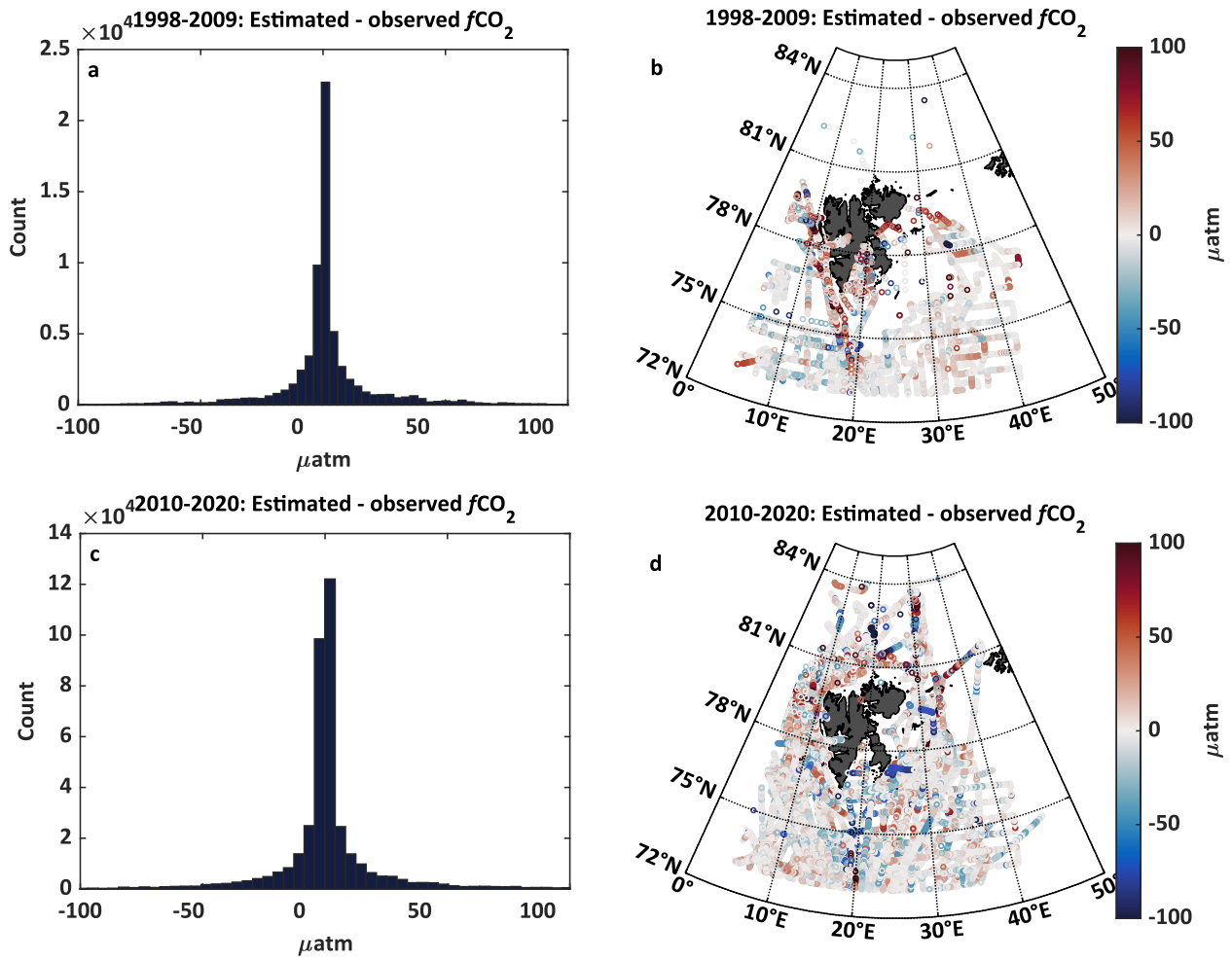

Fig. 12. (a) Histogram showing the distribution of the differences between estimated and observed fCO_2 before 2010, (b) the spatial distribution of the differences between estimated and observed fCO_2 before 2010, (c) histogram showing the distribution of the differences between estimated and observed fCO_2 from 2010 to 2020, (d) the spatial distribution of the differences between estimated and observed fCO_2 from 2010 to 2020.

Sea has been documented by Lind et al. (2018), and this is also an area where there were significantly increasing trends in the TOPAZ reanalysis MLD data (Fig. 9a-d, B4a-d). Vertical mixing has been documented to contribute to especially strong surface water trends in fCO_2 of + 3.6 to + 4.7 μatm yr^{-1} in the Southern Ocean (Metzl, 2009). Lind et al. (2018) also observed an increase in salinity in the northern Barents Sea, which again was captured in the TOPAZ reanalysis data (Fig. 8a-d). The increase in salinity is likely a signal of more AW, either advected or mixed up from below (Smedsrud et al., 2022), but can also result from brine-impacted deep water that is brought to surface through vertical mixing. Both AW and brine-influenced deep water will add more CO_2 to the surface layer. For instance, a shift from ArW to AW can result in an increase in fCO_2 from about 30 to>100 μatm depending on the season and year (Fig. 5a-l). On the other hand, AW contains higher nutrient concentrations, which may contribute to increased primary production as suggested by Randelhoff et al. (2018). For instance, high nutrient load in the inflowing Pacific Water to the Chukchi Sea likely dampens the CO_2 rise in these waters (Ouyang et al., 2020). On the other hand, Ericson et al. (2019) estimated that an increased influence of AW resulted in a decreased net community production in Isfjorden on the west coast of Spitsbergen.

Finally, we observed a warming trend with the strongest increase rates in the southern and western parts of the study area. The warming rate in the northern Barents Sea (i.e., in box B) was between 0.01 and 0.04 °C yr^{-1}, except for the summer season when the rates were very weak. This warming will also add to the increase in fCO_2. One reason for the weak warming rate in the northernmost part, if the signal in SSS reflects a greater influence of AW, could be that some of the heat in the AW is lost to sea-ice melt in this region (e.g., Renner et al., 2018).

4.2. Evaluation of the technique

The SOM technique has proven to be a useful tool to map the surface water fCO_2, that under the right circumstances can perform better in terms of predictability than the often-used MLR calculations (Lefévre et al., 2005). Both methods have been used in the Barents Sea region (Lauvset et al., 2013; Yasunaka et al., 2016,2018; Becker et al., 2021), despite the scarcity of data collected in winter and from the northern and eastern parts. Although some attempts to compare the reliability of the methods using independent measurements have been conducted, these are not from areas within the Barents Sea where the data coverage is especially sparse such as in areas with high ice concentrations (e.g., Lauvset et al., 2013). Consequently, it is difficult to properly validate these tools for the entire Barents Sea region, especially back in time when the data are considerably sparser. This is quite important, in particular considering that the present study found opposing changes to those found by Becker et al. (2021) in the northern Barents Sea. Here we used a K-fold cross-validation, that accounts for the spatiotemporal distribution of the labelling data set, to test the model performance. The estimated mean R^2, RMSE, and ME were 0.61, 30.5 μatm, and 0.54, respectively (Table 6). Altogether the model performance results are comparable to the results of Lauvset et al. (2013). Their independent

data tests gave ME estimates of 0.33 and 0.64. The former can be considered as a poor model result (<0.50), but the latter is good (0.5–0.65, Marechal, 2004). Interestingly, the RMSE of the poor model result was about 4.7 μatm compared to 19.3 μatm for the good result, reflecting that the ME evaluates the model performance relative to the variability in the observations it is trying to reproduce. The high RMSE in the present study can reflect a higher amount of data collected in waters with sea ice. Apart from uncertainties in the pairing of surface fCO_2 measurements to satellite sea ice concentrations, it should also be noted that during the sea-ice melt season underway measurements can overestimate the actual surface water fCO_2 due to a collection bias (Dong et al., 2021). I.e., the uppermost freshened surface layer that potentially lowers the surface fCO_2 is not sampled at the ship's inlet (Dong et al., 2021). For the entire data labelling set, the method performance in waters with sea ice was considerably poorer (see Table 5, R2 = 0.62, RMSE = 31.6 μatm, ME = 0.57) compared to the situation for open waters (R^2 = 0.77, RMSE = 18.8 μatm, ME = 0.76). We also note the overall the difference in sample points used in this study with close to half a million data points compared to about ten thousand in Lauvset et al. (2013) as well as the different time scales of the two studies.

Becker et al. (2021) showed that a higher amount of data can increase the variability and consequently increase the RMSE and decrease the R^2. In their study the highest amount of data used to construct the MLR algorithms, also resulted in the highest RMSE, perhaps not surprising for the complex dynamics of the Baltic Sea, but more intriguing when comparing the results in the well-studied North Sea to the results in the Barents Sea. In Becker et al. (2021), all MLR algorithms provided R^2, RMSE, and method efficiency values that supported better model fits for the Barents Sea compared to the North Sea, that had nearly three times as many data points. The unrealistic fCO_2 values found in the north-eastern areas of the Barents Sea with little data (Becker et al., 2021), do illustrate the sensitivity of skill assessment parameters to data abundance and distribution. Consequently, parameters such as R^2 and RMSE do not adequately capture the uncertainty in predicted data when data are especially sparse and should be handled with care when uncertainty estimates are the goal. The gridding of fCO_2 data used to produce either MLR relationships or SOMs also removes much of the variability, which for a dynamic and sea-ice influenced region such as the Barents Sea could be important to maintain. Yasunaka et al. (2018) obtained a R^2 value of 0.82 and a RMSE of 30 μatm in their SOM based mapping study of the Arctic Ocean. However, Yasunaka et al. (2016;2018) not only gridded the fCO_2 data but also removed extreme but potentially correct values to remove small-scale variability from the large-scale scope of their study. Here we chose to maintain the variability in the labelling data set, although acknowledging that for neurons with many fCO_2 labels only the most common is maintained, and used more than three times as many neurons in our SOM as Yasunaka et al. (2016;2018) used for the entire Arctic Ocean, to capture as much of the variability in the Barents Sea that was possible.

One of the strengths with the SOM technique, although also a limitation, is that the method cannot predict fCO_2 under conditions that it is not trained and labelled for. Consequently, to perform well the method requires training and labelling data sets that are fully representative for the region. In the present study, a large fraction of the neurons lacked labels (i.e., only 33 % were labelled with a fCO_2 value). Using smaller size of the SOM would have increased the labelling success of the neurons and the subsequent labelling of the weekly gridded fields, but at the cost of the representation of the variability in the area. Consequently, we choose to seasonally average the produced surface water fCO_2 maps and the resultant maps did show features in the Barents Sea that captured the dynamic structure of this oceanic region, such as the Polar Front. The averaging procedure may introduce potential biases as it is only the labelled neurons that are represented in the resultant map. Since the lack of labels reflect the lack of fCO_2 data under specific conditions, it is difficult to assess the resultant error. Another means to come around the problem with neurons that lack labels is to use the closest labelled neuron instead as was done by Yasunaka et al., (2018). This will allow for a 100 % label coverage but may introduce other biases in the resultant fCO_2 maps. All of this is difficult to assess. In contrast, the MLR method can extrapolate beyond the underlying data used to construct the algorithm. This can lead to unrealistic fCO_2 values in areas where the data are scarce. For instance, Becker et al., (2021) obtained very low and even negative fCO_2 values in the northern parts of the Barents Sea. This also relates to the assumption of linear relationships that underly the MLR approach. This is not necessarily valid. An example of this is the use of Chl *a* as predictor. When the spring bloom is initiated, Chl *a* increases while the fCO_2 decreases due to the consumption of CO_2 by the primary producers (Fransson et al., 2017). Typically, the peak values in Chl *a* extends over a couple of weeks (e.g., Wiedmann et al., 2016; Fransson et al., 2017). On the other hand, the fCO_2 will remain low over the entire summer season (e.g., Olsen et al., 2008; Ericson et al., 2018;2019) and can consequently be associated with both high and low Chl *a*. This feature relates to the difference in timescales between phytoplankton blooms and air-sea CO_2 uptake. The latter acts over months and will slowly replenish the surface water with CO_2.

To handle the lack of fCO_2 measurements in ice-covered waters, we encourage more studies to utilize the ever increasing number of fCO_2 measurements to challenge the prevailing maps, using either the SOM technique or the MLR algorithms. We also acknowledge that the lack of data back in time results in the fact that fCO_2 cannot easily be reconstructed and properly validated historically regardless of the accumulation of recent fCO_2 measurements. This is an important note since the Barents Sea has changed substantially over the last four decades. Both changes in the sea-ice distribution and composition, e.g., the ice edge has moved northwards, and the multiyear ice has largely been replaced by first year ice, will affect the CO_2 cycling. Therefore, using sea-ice conditions in the last decade to reconstruct historic fCO_2 can introduce substantial biases.

5. Future perspectives

For the first time, strong increasing trends in the surface water fCO_2 are shown to occur in the northern Barents Sea and southern Nansen Basin. These trends take place in an area where the sea ice is quickly diminishing, and the AW is expanding, and confirms that sea ice has a strong impact on the oceanic uptake of CO_2. The increases in the surface water fCO_2 result in a reduced oceanic uptake capacity for atmospheric CO_2 and a lowered surface water pH (i.e., dissolved CO_2 reacts with water to dissociate into bicarbonate and a proton). Consequently, it is expected that ocean acidification is speeding up in this already vulnerable area, with consequences for the planktonic communities. Especially note that the strong trends are observed in the winter to summer seasons when many organisms reproduce.

The differences found in the temporal evolution of the estimated surface water fCO_2 in the northern Barents Sea between the present study and that of Becker et al. (2021), makes it also abundantly clear that the current mapping techniques are sensitive to the lack of data in this area. More in situ fCO_2 measurements in winter and spring when the sea ice cover is more extensive, will enhance the capacity of the SOM technique to estimate the surface fCO_2. This requires that the ice-going vessels manage to maintain an open seawater intake in ice-covered waters, which is not always the case. The spatial patchiness and often time-limited distribution of blooming algae also requires frequent underway measurements over the spring season. Regardless, the SOM

technique applied in the present study, cannot fill all missing knowledge back in time, but it still manages impressively well to capture fCO_2 variability associated with known physical and biogeochemical features in the eastern Fram Strait and north-western Barents Sea area, including the dynamic Polar Front. The technique is also sensitive enough to detect changes in fCO_2 which will help to provide more knowledge on drivers of climate change in the rapidly changing High North.

6. Data availability

The SOCATv2021 and the R/V Lance data can be downloaded at https://www.socat.info, note that the latter are flagged with E and not included in some of the products. The Kronprins Haakon data are available in the Norwegian Polar Data Centre (https://doi.org/10.21334/npolar.2023.8e0afb8b). Data from GLODAPv2.2021 are available at https://www.glodap.info. Data from CARINA are available at https://www.ncei.noaa.gov/access/ocean-carbon-acidification-data-system/oceans/CARINA/. Finally, the remaining cruise data are from: Chierici & Fransson (2019, https://doi.org/10.21335/NMDC-154415697), Chierici et al. (2022, https://doi.org/10.21335/NMDC-1341949456), Chierici et al. (2019, https://doi.org/10.21335/NMDC-1738969988), and Jones et al. (2021, https://doi.org/10.1016/j.pocean.2021.102708).

Declaration of Competing Interest

The authors declare that they have no known competing financial interests or personal relationships that could have appeared to influence the work reported in this paper.

Data availability

All data sets are referenced to.

Acknowledgement

This study was funded from the Research Council of Norway through several projects including the Nansen Legacy project (RCN # 276730), "Integrated Carbon Observing System" Norway phase 1 (RCN # 245927) and phase 2 (RCN # 296012). In addition, the study was funded through the Norwegian Environment Agency projects Monitoring Ocean Acidification 2014, 2015, 2016 (#s 14098027, 15078033, 16078007) and Ocean Acidification Program 2016-2020 (# 17078007). Furthermore, the study was also funded through the EU Horizon 2020 project "Our common future ocean in the Earth system – quantifying coupled cycles of carbon, oxygen, and nutrients for determining and achieving safe operating spaces with respect to tipping points" (COMFORT – EU project number # 820989).

The study has been conducted using E.U. Copernicus Marine Service Information (https://doi.org/10.48670/moi-00007, https://doi.org/10.48670/moi-00052). The SOM Toolbox version 2.1 developed for Matlab 5 used in the present study was created and is freely distributed by the SOM Toolbox team (i.e., Esa Alhoniemi, Johan Himberg, Jukka Parviainen and Juha Vesanto) at the Aalto University, Department of Department of Information and Computer Science, Aalto, Finland. Finally, the authors gratefully acknowledge the valuable comments and suggestions from two anonymous reviewers.

Appendix A:. Salinity bias

Monthly mean maps from the Arctic Ocean Physics Reanalysis product based on the TOPAZ4 model and the Global Ocean Observation-based Products (MULTIOBS) are shown to clarify where the bias of water with lower salinities in the World Ocean Atlas 2018 affects the two data sets (see Figs. A1 and A2).

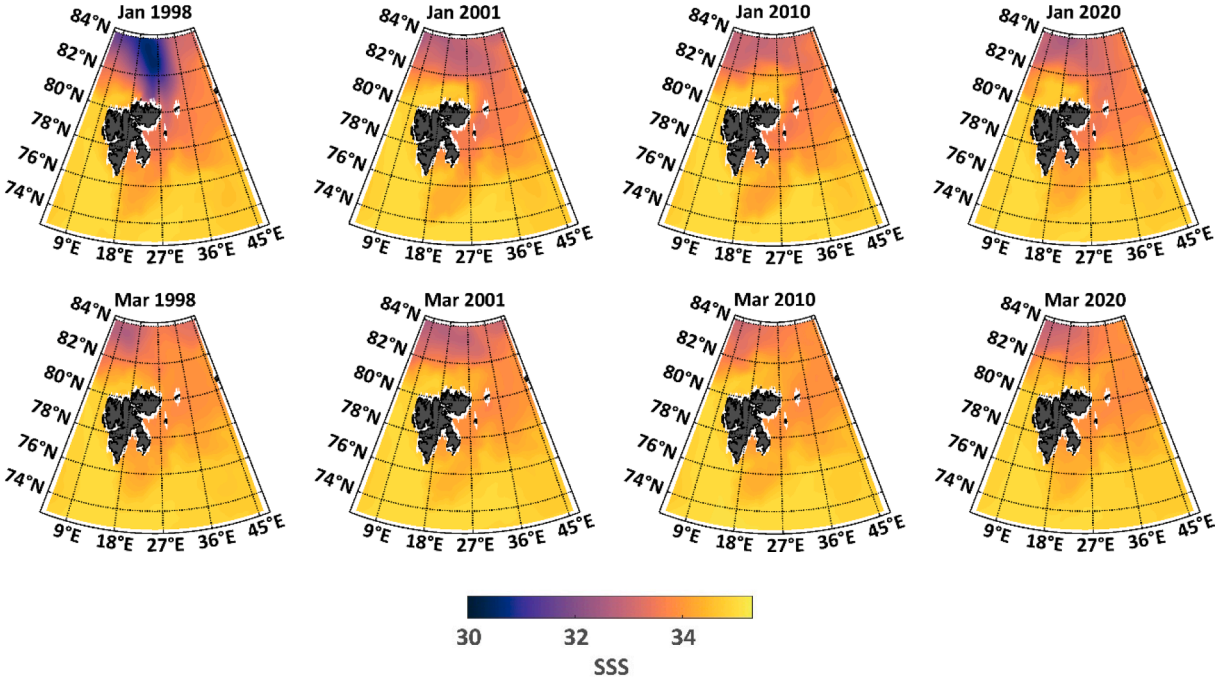

Fig. A1. Monthly mean SSS from the Arctic Ocean Physics Reanalysis product based on the TOPAZ4 model.

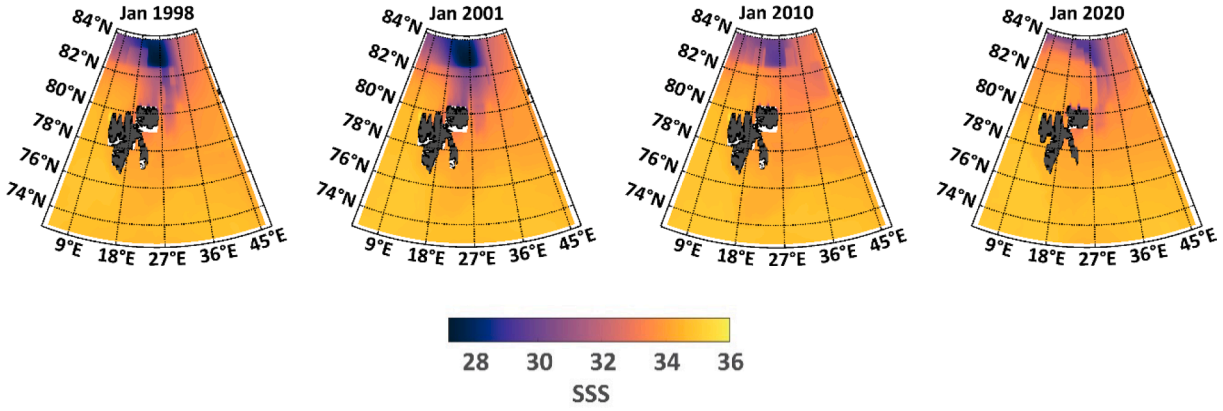

Fig. A2. Monthly mean SSS sampled at 10 m from the Global Ocean Observation-based Products (MULTIOBS).

Appendix B:. p values

Figs. B1-B6.

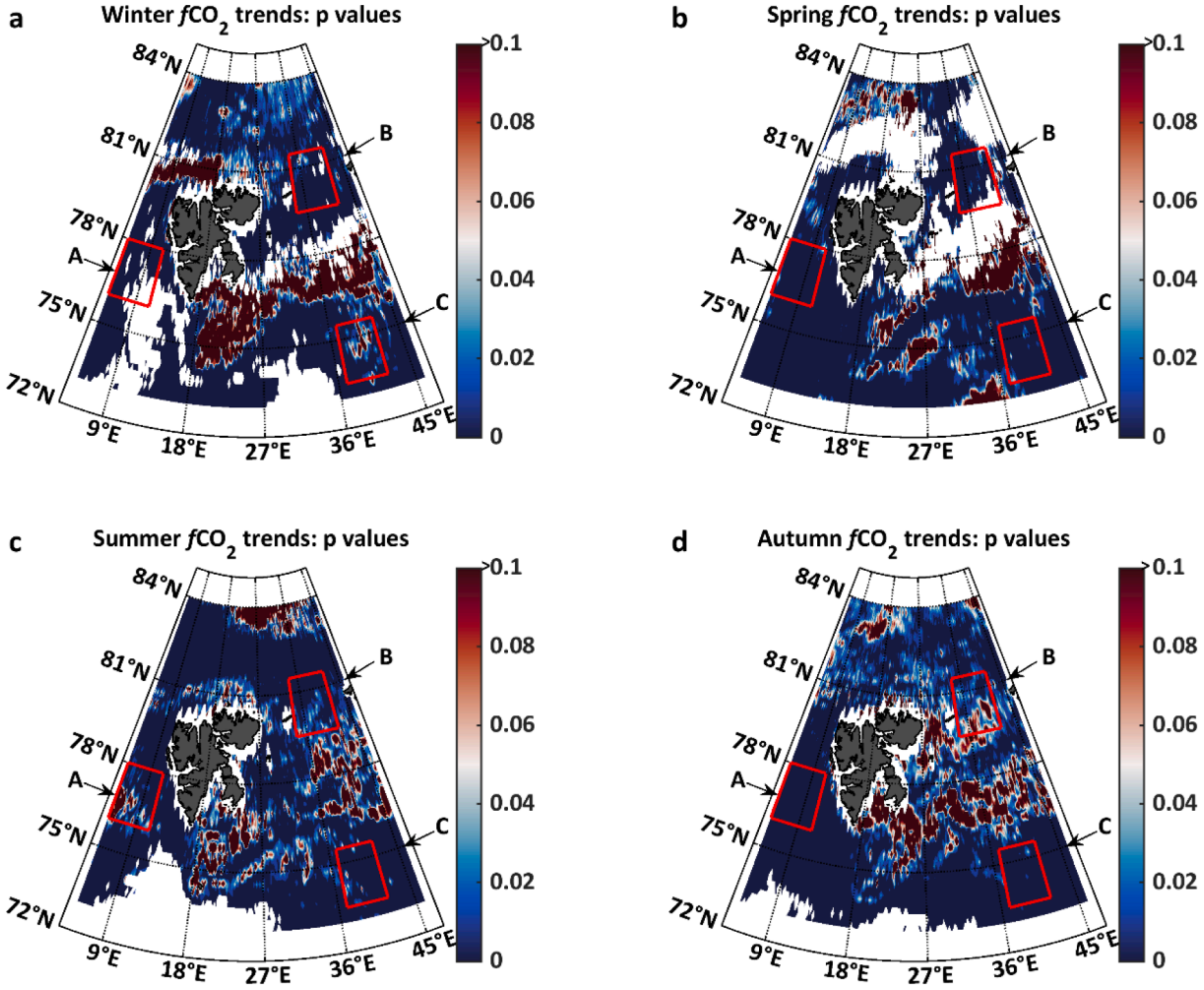

Fig. B1. P values of trends in surface water fCO_2 in **a)** winter, **b)** spring, **c)** summer, and **d)** autumn. Null hypothesis is that no relationship between the estimated seasonal fCO_2 and time in years exist. Boxes A, B, and C, were used to spatially average the trends.

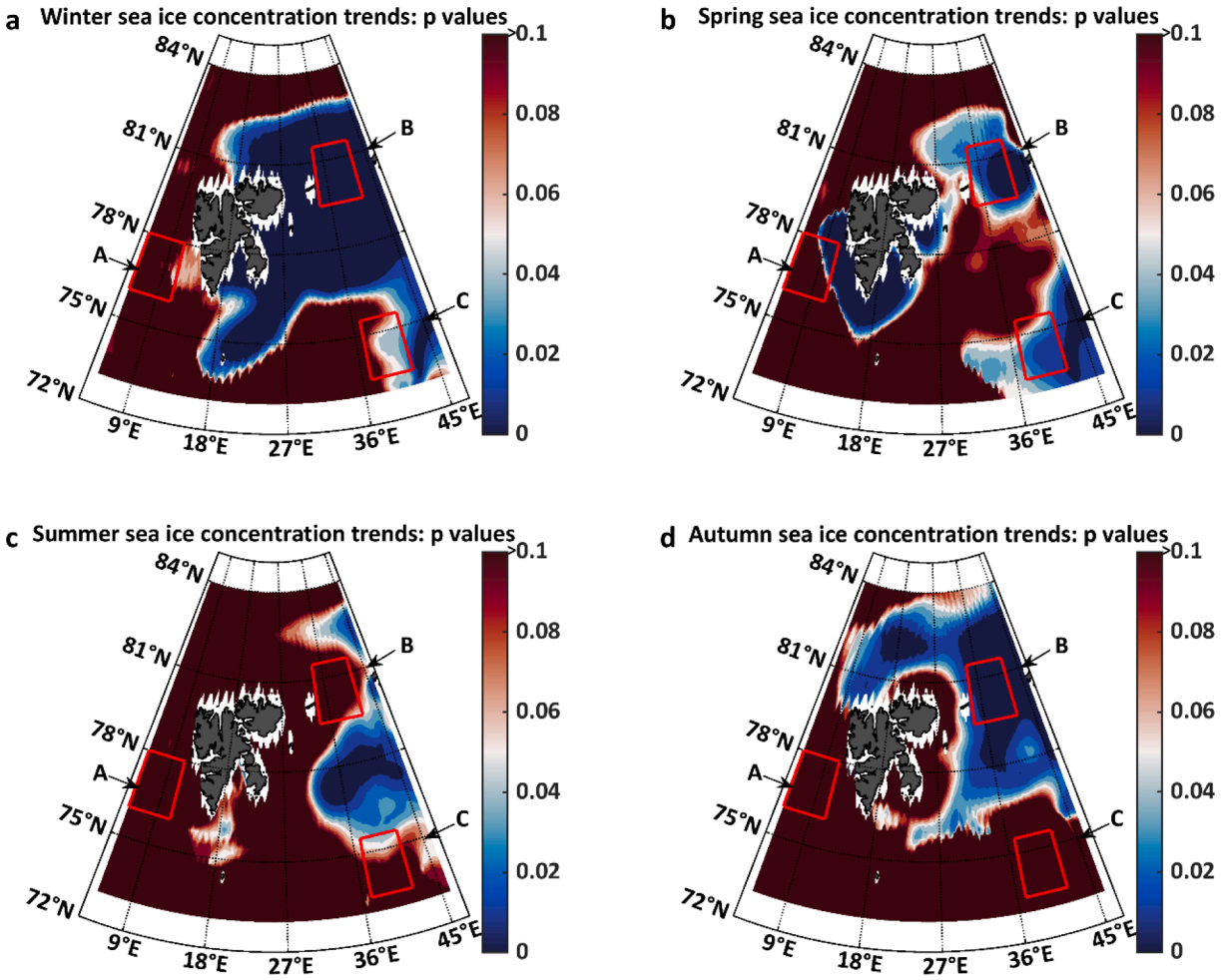

Fig. B2. P values of trends in sea ice concentration in **a)** winter, **b)** spring, **c)** summer, and **d)** autumn. Null hypothesis is that no relationship between the seasonal sea ice concentration and time in years exist.

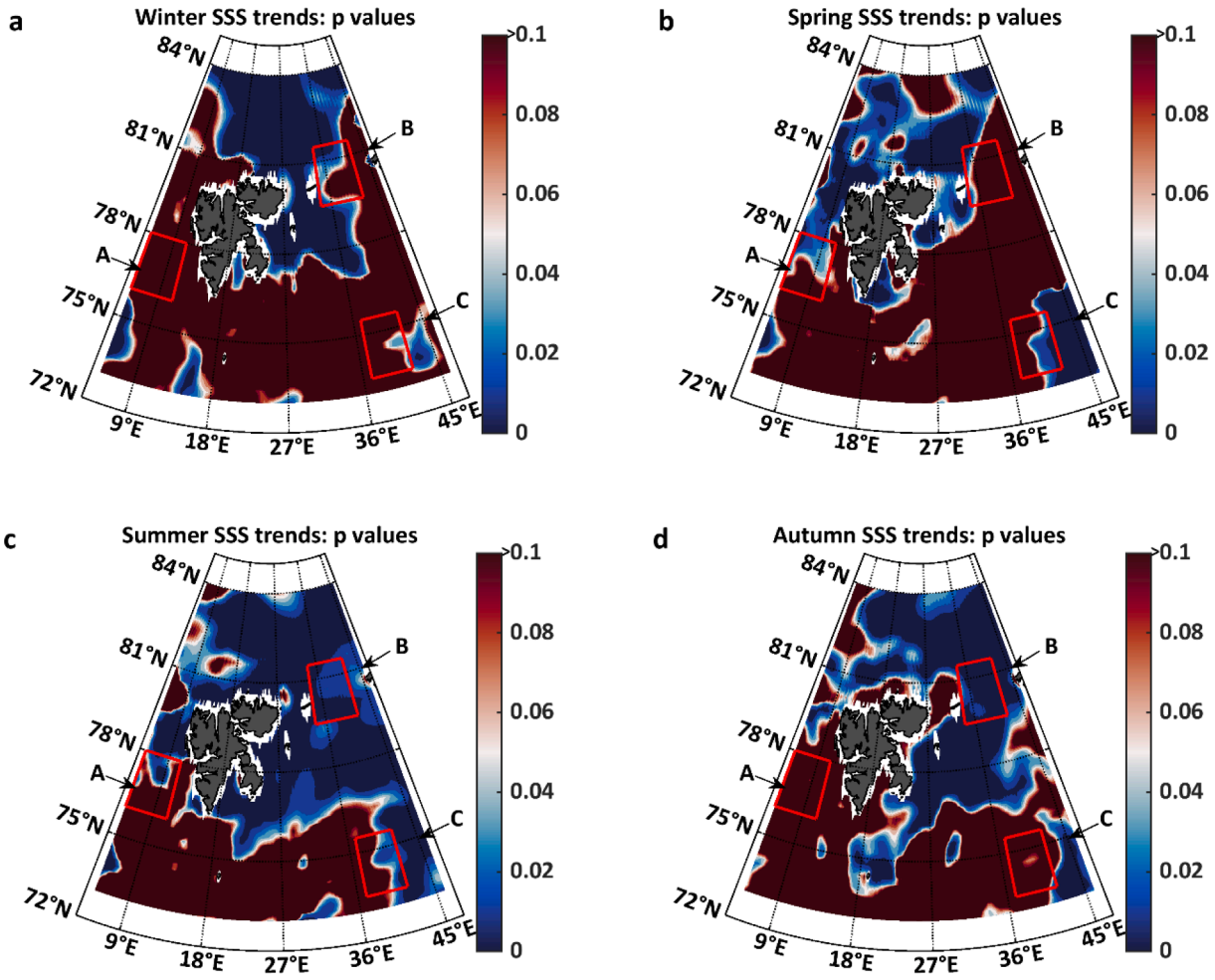

Fig. B3. P values of trends in SSS in **a)** winter, **b)** spring, **c)** summer, and **d)** autumn. Null hypothesis is that no relationship between the seasonal SSS and time in years exist.

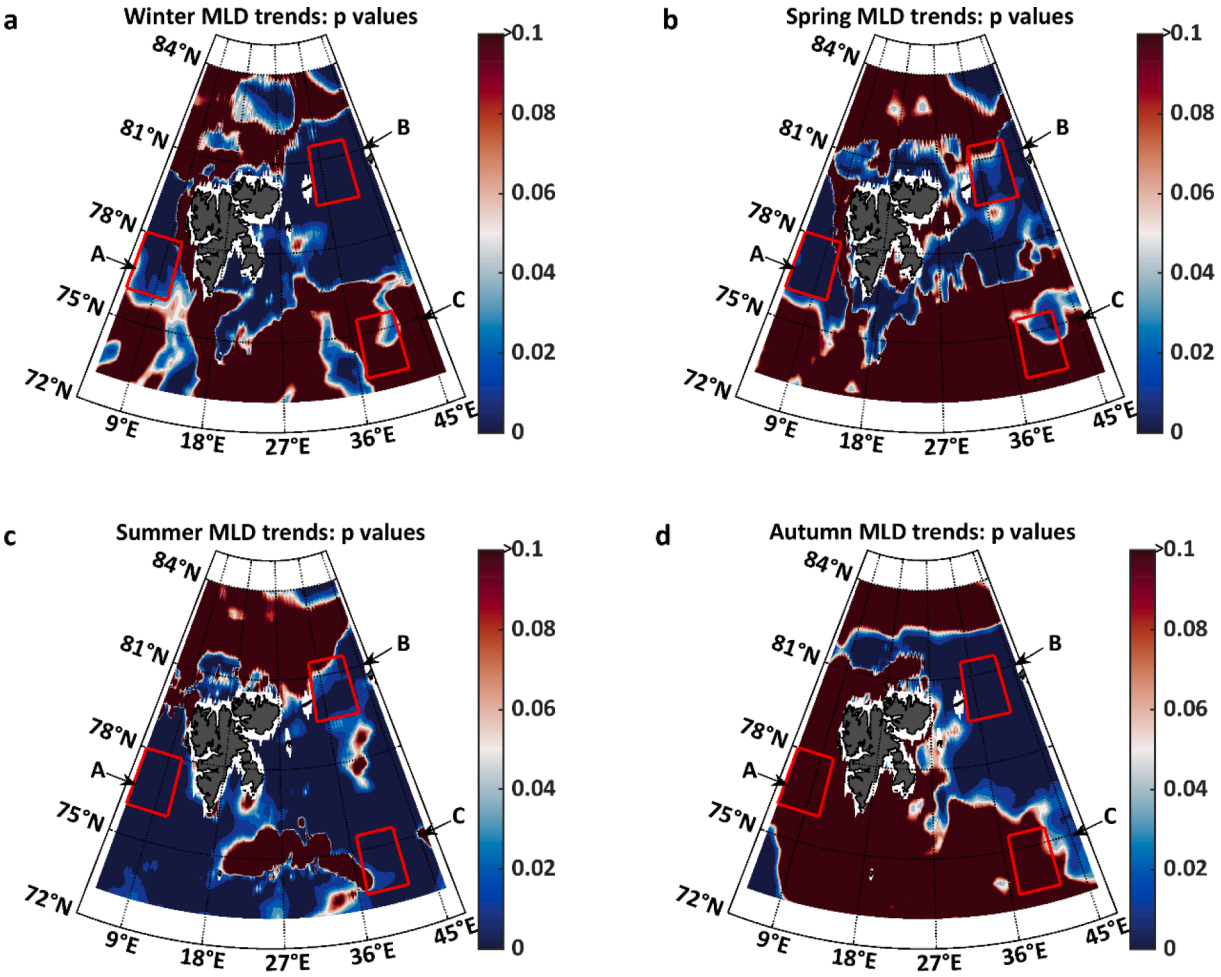

Fig. B4. P values of trends in MLD in **a)** winter, **b)** spring, **c)** summer, and **d)** autumn. Null hypothesis is that no relationship between the seasonal MLD and time in years exist.

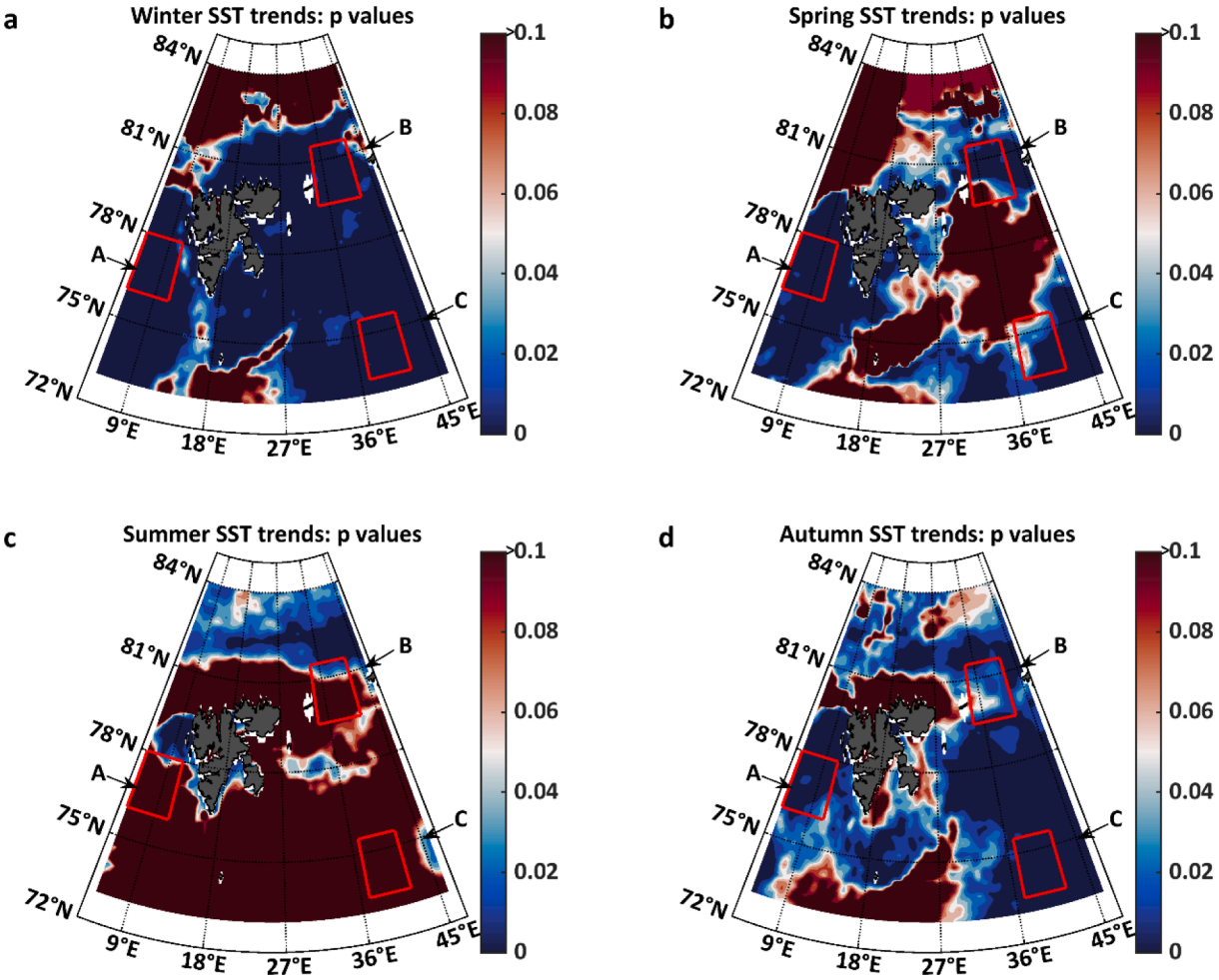

Fig. B5. P values of trends in SST in **a)** winter, **b)** spring, **c)** summer, and **d)** autumn. Null hypothesis is that no relationship between the seasonal SST and time in years exist.

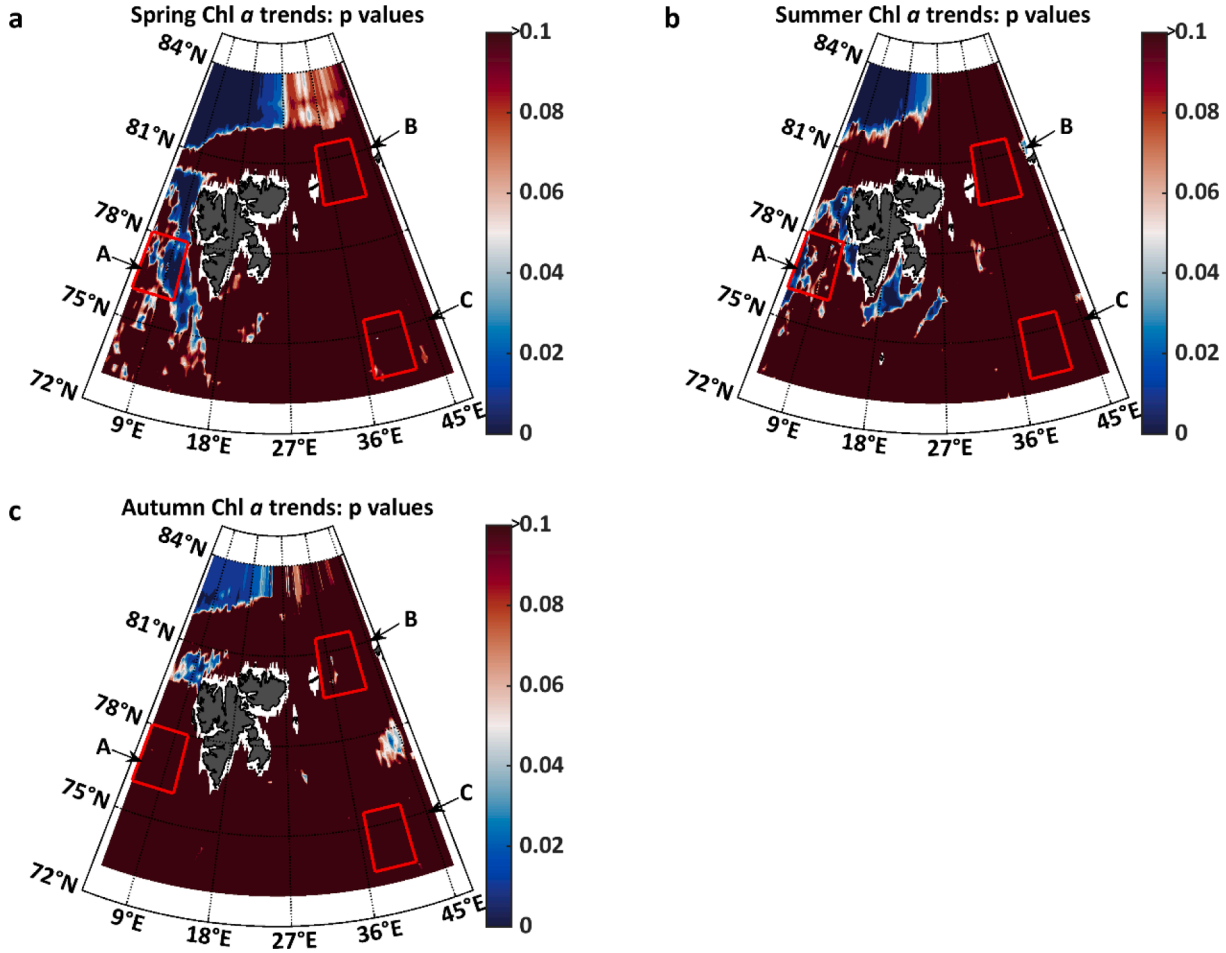

Fig. B6. P values of trends in Chl *a* in **a)** spring, **b)** summer, and **c)** autumn. Null hypothesis is that no relationship between the seasonal Chl *a* and time in years exist.

References

Årthun, M., Eldevik, T., Smedsrud, L.H., Skagseth, Ø., Ingvaldsen, R.B., 2012. Quantifying the influence of Atlantic heat on Barents Sea ice variability and retreat. J. Clim. 25, 4736–4743. https://doi.org/10.1175/JCLI-D-11-00466.1.

Bakker, D.C.E., Pfeil, B., Landa, C.S., Metzl, N., O'Brien, K.M., Olsen, A., Smith, K., Cosca, C., et al., 2016. A multi-decade record of high quality fCO_2 data in version 3 of the Surface Ocean CO_2 Atlas (SOCAT). Earth Syst. Sci. Data 8, 383–413. https://doi.org/10.5194/essd-8-383-2016.

Becker, M., Olsen, A., Landschützer, P., Omar, A., Rehder, G., Rödenbeck, C., Skjelvan, I., 2021. The norther European shelf as an increasing net sink for CO_2. Biogeosciences 18, 1127–1147. https://doi.org/10.5194/bg-18-1127-2021.

Cao, Y., Cervone, G., Barkley, Z., Lauvaux, T., Deng, A., Taylor, A., 2017. Analysis of errors introduced by geographic coordinate systems on weather numeric prediction modeling. Geosci. Model Dev. 10, 3425–3440. https://doi.org/10.5194/gmd-10-3425-2017.

Chierici, M., Fransson, A., 2019. Seasonal variability of the marine CO_2 system and nutrients in the Atlantic water inflow to the Arctic Ocean in 2014. doi:10.21335/NMDC-154415697.

Chierici, M., Jones, E., Hodal Lødemel, H., 2019. Interannual variability of the marine CO_2 system and nutrients in the Barents Sea from 2011 to 2017. 10.21335/NMDC-1738969988.

Chierici, M., Reigstad, M., Hodal Lødemel, H., Kristiansen, S., 2022a. Spatial variability of the marine CO_2 system and inorganic nutrients in the water column along the Vardø-North section in the Barents Sea to the Nansen Basin, Arctic Ocean in September 2012. 10.21335/NMDC-1341949456.

Dickson, A.G., 1990. Standard potential of the reaction: $AgCl(s) + 1/2H_2(g) = Ag(s) + HCl(aq)$, and the standard acidity constant of the ion HSO_4^- in synthetic sea water from 273.15 to 318.15 K. J. Chem. Thermodyn. 22, 113–127. https://doi.org/10.1016/0021-9614(90)90074-Z.

Dickson, A.G., Millero, F.J., 1987. A comparison of the equilibrium constants for the dissociation of carbonic acid in seawater media. Deep Sea Res. Part A 34 (10), 1733–1743. https://doi.org/10.1016/0198-0149(87)90021-5.

Dlugokencky, E.J., Mund, J.W., Crotwell, A.M., Crotwell, M.J., Thoning, K.W., 2021. Atmospheric Carbon Dioxide Dry Air Mole Fractions from the NOAA GML Carbon Cycle Cooperative Global Air Sampling Network, 1968-2020, Version: 2021-07-30. 10.15138/wkgj-f215.

Dong, Y., Yang, M., Bakker, D.C.E., Liss, P.S., Kitidis, V., Brown, I., et al., 2021. Near-surface stratification due to ice melt biases Arctic air-sea CO_2 flux estimates. Geophys. Res. Lett. 48 https://doi.org/10.1029/2021GL095266 e2021GL095266.

Ericson, Y., Falck, E., Chierici, M., Fransson, A., Kristiansen, S., Platt, S.M., et al., 2018. Temporal variability in surface water pCO_2 in Adventfjorden (West Spitsbergen) with emphasis on physical and biogeochemical drivers. J. Geophys. Res. Oceans 123. https://doi.org/10.1029/2018JC014073.

Ericson, Y., Chierici, M., Falck, E., Fransson, A., Jones, E., Kristiansen, S., 2019. Seasonal dynamics of the marine CO_2 system in Adventfjorden, a west Spitsbergen fjord. Polar Res. 38, 3345. https://doi.org/10.33265/polar.v38.3345.

Fransner, F., Fröb, F., Tjiputra, J., Goris, N., Lauvset, S.K., Skjelvan, I., Jeansson, E., Omar, A., Chierici, M., Jones, E., Fransson, A., Ólafsdóttir, S.R., Johannessen, T., Olsen, A., 2022. Acidification of the Nordic Seas. Biogeosciences 19, 979–1012. https://doi.org/10.5194/bg-19-979-2022.

Fransson A., Chierici, M., Skjelvan, I., Olsen, A., Assmy, P., A. Peterson, G. Spreen, G., Ward, B., 2017. Effect of sea-ice and biogeochemical processes and storms on under-ice water fCO_2 during the winter-spring transition in the high Arctic Ocean: implications for sea-air CO_2 fluxes. JGR- Oceans, N-ICE special issue, doi: 10.1002/2016JC012478.

Fransson, A., Ericson, Y., Chierici, M., 2023. Surface water fCO_2 in the Barents Sea and Nansen Basin. 10.21334/npolar.2023.8e0afb8b.

Garnesson, P., Mangin, A., Fanton d'Andon, O., Demaria, J., Bretagnon, M., 2019. The CMEMS GlobColour chlorophyll a product based on satellite observation: multi-sensor merging and flagging strategies. Ocean Sci. 15, 819–830. https://doi.org/10.5194/os-15-819-2019.

[dataset] Good, S.A., Embury, O., Bulgin, C.E., Mittaz, J., 2019. ESA Sea Surface Temperature Climate Change Initiative (SST_cci): Level 4 Analysis Climate Data Record, version 2.0. Centre for Environmental Data Analysis. https://doi.org/10.5285/aced40d7cb964f23a0fd3e85772f2d48.

Graham, R.M., Itkin, P., Meyer, A., et al., 2019. Winter storms accelerate the demise of sea ice in the Atlantic sector of the Arctic Ocean. Sci. Rep. 9, 9222. https://doi.org/10.1038/s41598-019-45574-5.

Hauck, J., Nissen, C., Landschützer, P., Rödenbeck, C., Bushinsky, S., Olsen, A., 2023. Sparse observations induce large biases in estimates of the global ocean CO_2 sink: an ocean model subsampling experiment. Phil. Trans. R. Soc. A 381, 20220063. https://doi.org/10.1098/rsta.2022.0063.

Henley, S.F., Porter, M., Hobbs, L., Braun, J., Guillaume-Castel, R., Venables, E.J., Dumont, E., Cottier, F., 2020. Nitrate supply and uptake in the Atlantic Arctic sea ice zone: seasonal cycle, mechanisms and drivers. Phil. Trans. R. Soc. A 378, 20190361. https://doi.org/10.1098/rsta.2019.0361.

Ingvaldsen, R.B., Assmann, K.M., Primicerio, R., et al., 2021. Physical manifestations and ecological implications of Arctic Atlantification. Nat. Rev. Earth Environ. 2, 874–889. https://doi.org/10.1038/s43017-021-00228-x.

Jones, E., Chierici, M., Menze, S., Fransson, A., Ingvaldsen, R.B., Hodal Lødemel, H., 2021. Ocean acidification state variability of the Atlantic Arctic Ocean around northern Svalbard. Prog. Oceanogr. https://doi.org/10.1016/j.pocean.2021.102708.

Jutterström, S., Anderson, L.G., Bates, N.R., Bellerby, R., Johannessen, T., Jones, E.P., Key, R.M., Lin, X., Olsen, A., Omar, A.M., 2010. Arctic Ocean data in CARINA. Earth Sys. Sci. Data 2, 71–78.

Key, R.M., Tanhua, T., Olsen, A., Hoppema, M., Jutterström, S., Schirnick, C., van Heuven, S., Kozyr, A., Lin, X., Velo, A., Wallace, D.W.R., Mintrop, L., 2010. The CARINA data synthesis project: Introduction and overview. Earth Sys. Sci. Data 2, 105–121.

Kohonen, T., 2001. Self-Organizing Maps. Third ed. Springer Series in Information Sciences, vol. 30. Springer-Verlag Berlin, Heidelberg. 502 pp. 10.1007/978-3-642-56927-2.

Kwok, R., 2018. Arctic sea ice thickness, volume, and multiyear ice coverage: losses and coupled variability (1958–2018). Environ. Res. Lett. 13, 105005.

Kwok, R., Maslowski, W., Laxon, S.W., 2005. On large outflows of Arctic sea ice into the Barents Sea. Geophys. Res. Lett. 32, L22503. https://doi.org/10.1029/2005GL024485.

Landschützer, P., Gruber, N., Bakker, D.C.E., Schuster, U., Nakaoka, S., Payne, M.R., Sasse, T.P., Zeng, J., 2013. A neural network-based estimate of the seasonal to inter-annual variability of the Atlantic Ocean carbon sink. Biogeosciences 10, 7793–7815. https://doi.org/10.5194/bg-10-7793-2013.

Laruelle, G.G., Landschützer, P., Gruber, N., Tison, J.-L., Delille, B., Regnier, P., 2017. Global high-resolution monthly pCO_2 climatology for the coastal ocean derived from neural network interpolation. Biogeosciences 14, 4545–4561. https://doi.org/10.5194/bg-14-4545-2017.

Lauvset, S.K., Chierici, M., Counillon, F., Omar, A., Nondal, G., Johannessen, T., Olsen, A., 2013. Annual and seasonal fCO_2 and air–sea CO_2 fluxes in the Barents Sea. J. Mar. Syst. 113–114, 62–74. https://doi.org/10.1016/j.jmarsys.2012.12.011.

Lauvset, S.K., Lange, N., Tanhua, T., Bittig, H.C., Olsen, A., Kozyr, A., Álvarez, M., Becker, S., Brown, P.J., Carter, B.R., Cotrim da Cunha, L., Feely, R.A., van Heuven, S., Hoppema, M., Ishii, M., Jeansson, E., Jutterström, S., Jones, S.D., Karlsen, M.K., Lo Monaco, C., Michaelis, P., Murata, A., Pérez, F.F., Pfeil, B., Schirnick, C., Steinfeldt, R., Suzuki, T., Tilbrook, B., Velo, A., Wanninkhof, R., Woosley, R.J., Key, R.M., 2021. An updated version of the global interior ocean biogeochemical data product, GLODAPv2.2021. Earth Syst. Sci. Data 13, 5565–5589. https://doi.org/10.5194/essd-13-5565-2021.

Lavergne, T., Sørensen, A.M., Kern, S., Tonboe, R., Notz, D., Aaboe, S., Bell, L., Dybkjær, G., Eastwood, S., Gabarro, C., Heygster, G., Killie, M.A., Brandt Kreiner, M., Lavelle, J., Saldo, R., Sandven, S., Pedersen, L.T., 2019. Version 2 of the EUMETSAT OSI SAF and ESA CCI sea-ice concentration climate data records. Cryosphere 13, 49–78. https://doi.org/10.5194/tc-13-49-2019.

Lee, K., Kim, T.-W., Byrne, R.H., Millero, F.J., Feely, R.A., Liu, Y.-M., 2010. The universal ratio of boron to chlorinity for the North Pacific and North Atlantic oceans. Geochem. Cosmochim. Acta 74, 1801–1811.

Lefévre, N., Watson, A.J., Watson, A.R., 2005. A comparison of multiple regression and neural network techniques for mapping in situ pCO_2 data. Tellus B: Chem. Phys. Meteorol. 57 (5), 375–384. https://doi.org/10.3402/tellusb.v57i5.16565.

Lewis, K.M., van Dijken, G.L., Arrigo, K.R., 2020. Changes in phytoplankton concentration now drive increased Arctic Ocean primary production. Science 369, 198–202. https://doi.org/10.1126/science.aay8380.

Lind, S., Ingvaldsen, R.B., Furevik, T., 2018. Arctic warming hotspot in the northern Barents Sea linked to declining sea-ice import. Nat. Clim. Chang. 8, 634–639. https://doi.org/10.1038/s41558-018-0205-y.

Mehrbach, C., Culberson, C.H., Hawley, J.E., Pytkowicz, R.M., 1973. Measurement of the apparent dissociation constants of carbonic acid in seawater at atmospheric pressure. Limnol. Oceanogr. 18, 897–907. https://doi.org/10.4319/lo.1973.18.6.0897.

Merchant, C.J., Embury, O., Bulgin, C.E., et al., 2019. Satellite-based time-series of sea-surface temperature since 1981 for climate applications. Sci. Data 6, 223. https://doi.org/10.1038/s41597-019-0236-x.

Metzl, N., 2009. Decadal increase of oceanic carbon dioxide in southern Indian surface waters (1991–2007). Deep Sea Res. Part II 56, 607–619. https://doi.org/10.1016/j.dsr2.2008.12.007.

Olsen, A., Brown, K.R., Chierici, M., Johannessen, T., Neill, C., 2008. Sea-surface CO_2 fugacity in the subpolar North Atlantic. Biogeosciences 5, 535–547. https://bg.copernicus.org/articles/5/535/2008/.

Omar, A.M., Johannessen, T., Olsen, A., Kaltin, S., Rey, F., 2007. Seasonal and interannual variability of the air–sea CO_2 flux in the Atlantic sector of the Barents Sea. Mar. Chem. 104 (3–4), 203–213. https://doi.org/10.1016/j.marchem.2006.11.002.

Orr, J.C., Epitalon, J.-M., Dickson, A.G., Gattuso, J.-P., 2018. Routine uncertainty propagation for the marine carbon dioxide system, in prep. for Mar. Chem. 207, 84–107. https://doi.org/10.1016/j.marchem.2018.10.006.

OSI SAF, 2017. Global Sea Ice Concentration Climate Data Record v2.0 - Multimission, EUMETSAT SAF on Ocean and Sea Ice, Norwegian and Danish Meteorological Institutes. doi: 10.15770/EUM_SAF_OSI_0008. https://doi.org/10.15770/EUM_SAF_OSI_0008.

Ouyang, Z., Qi, D., Chen, L., et al., 2020. Sea-ice loss amplifies summertime decadal CO_2 increase in the western Arctic Ocean. Nat. Clim. Chang. 10, 678–684. https://doi.org/10.1038/s41558-020-0784-2.

Pierrot, D., Neill, C., Sullivan, K., Castle, R., Wanninkhof, R., Lüger, H., Johannessen, T., Olsen, A., Feely, R.A., Cosca, C.E., 2009. Recommendations for autonomous underway pCO_2 measuring systems and data-reduction routines. Deep Sea Res. Part II 56 (8–10), 512–522. https://doi.org/10.1016/j.dsr2.2008.12.005.

Polyakov, I.V., Pnyushkov, A.V., Alkire, M.B., Ashik, I.M., Baumann, T.M., Carmack, E.C., Guthrie, J., Ivanov, V.V., Kanzow, T., Krishfield, R., Kwok, R., Sundfjord, A., Morison, J., Rember, R., Yulin, A., 2017. Greater role for Atlantic inflows on sea-ice loss in the Eurasian Basin of the Arctic Ocean. Science 356 (6335), 285–291. https://doi.org/10.1126/science.aai8820.

Qi, D., Ouyang, Z., Chen, L., Wu, Y., Lei, R., Chen, B., Feely, R.A., Anderson, L.G.A., Zhong, W., Lin, H., Polukhin, A., Zhang, Y., Zhang, Y., Bi, H., Lin, X., Luo, Y., Zhuang, Y., He, J., Chen, J., Cai, W.-J., 2022. Climate change drives rapid decadal acidification in the Arctic Ocean from 1994 to 2020. Science 377, 1544–1550. https://doi.org/10.1126/science.abo03.

Randelhoff, A., Reigstad, M., Chierici, M., Sundfjord, A., Ivanov, V., Cape, M., Vernet, M., Tremblay, J.-É., Bratbak, G., Kristiansen, S., 2018. Seasonality of the Physical and Biogeochemical Hydrography in the Inflow to the Arctic Ocean Through Fram Strait. Front. Mar. Sci. 5, 224. https://doi.org/10.3389/fmars.2018.00224.

Randelhoff, A., Lacour, L., Marec, C., Leymarie, E., Lagunas, J., Xing, X., Darnis, G., Penkerch, C., Sampei, M., Fortier, L., D'Ortenzio, F., Claustre, H., Babin, M., 2020. Arctic mid-winter phytoplankton growth revealed by autonomous profilers. Sci. Adv. 6, eabc2678.

Renner, A.H.H., Sundfjord, A., Janout, M.A., Ingvaldsen, R.B., Beszczynska-Möller, A., Picart, R.S., Pérez-Harnández, M.D., 2018. Variability and redistribution of heat in the Atlantic Water boundary current north of Svalbard. J. Geophys. Res. Oceans 123, 6373–6391. https://doi.org/10.1029/2018JC013814.

Rysgaard, S., Bendtsen, J., Delille, B., Dieckmann, G.S., Glud, R.N., Kennedy, H., Mortensen, J., Papadimitriou, S., Thomas, D.N., Tison, J.-L., 2011. Sea ice contribution to the air–sea CO_2 exchange in the Arctic and Southern Oceans. Tellus B: Chem. Phys. Meteorol. 63 (5), 823–830. https://doi.org/10.1111/j.1600-0889.2011.00571.x.

OSI SAF, 2019. Global sea ice concentration interim climate data record 2016 onwards (v2.0), EUMETSAT SAF on Ocean and Sea Ice, Norwegian and Danish Meteorological Institutes. See Lavergne et al. (2019).

Skagseth, Ø., Eldevik, T., Årthun, M., Asbjørnsen, H., Lien, V.S., Smedsrud, L.H., 2020. Reduced efficiency of the Barents Sea cooling machine. Nat. Clim. Chang. https://doi.org/10.1038/s41558-020-0772-6.

Skjelvan, I., Lauvset, S.K., Johannessen, T., Gundersen, K., Skagseth, Ø., 2022. Decadal trends in Ocean Acidification from the Ocean Weather Station M in the Norwegian Sea. J. Mar. Sys. 234 https://doi.org/10.1016/j.jmarsys.2022.103775.

Smedsrud, L.H., Muilwijk, M., Brakstad, A., Madonna, E., Lauvset, S.K., Spensberger, C., et al., 2022. Nordic Seas heat loss, Atlantic inflow, and Arctic sea ice cover over the last century. Rev. Geophys. 60 e2020RG000725.

Supply, A., Boutin, J., Vergely, J.-L., Kolodziejczyk, N., Reverdin, G., Reul, N., Tarasenko, A., 2020. New insights into SMOS sea surface salinity retrievals in the Arctic Ocean. Remote Sens. Environ. 249, 112027 https://doi.org/10.1016/j.rse.2020.112027.

Takahashi, T., Olafsson, J., Goddard, J.G., Chipman, D.W., Sutherland, S.C., 1993. Seasonal variation of CO_2 and nutrients in the high latitude surface oceans: A comparative study. Global Biogeochem. Cycles 7 (4), 843–878. https://doi.org/10.1029/93GB02263.

Telszewski, M., Chazottes, A., Schuster, U., Watson, A.J., Moulin, C., Bakker, D.C.E., Gonzalez-Davila, M., Johannessen, T., Körtzinger, A., Lüger, H., Olsen, A., Omar, A., Padin, X.A., Rios, A.F., Steinhoff, T., Santana-Casiano, M., Wallace, D.W.R., Wanninkhof, R., 2009. Estimating the monthly pCO_2 distribution in the North Atlantic using a self-organizing neural network. Biogeosciences 6, 1405–1421.

van Heuven, S., Pierrot, D., Rae, J.W.B., Lewis, E., Wallace, D.W.R., 2011. MATLAB Program Developed for CO2 System Calculations. ORNL/CDIAC-105b, Carbon Dioxide Information Analysis Center. Oak Ridge National Laboratory, Oak Ridge, Tennessee.

Vinje, T., Kvambekk, A., 1991. Barents Sea drift ice characteristics. Pp. 59-68 in Sakshaug, E., Hopkins., C.C.E., 0ritsland, N.A. (eds.). Proceedings of the Pro Mare Symposium on Polar Marine Ecology. Trondheim, 12-16 May 1990. Polar Research 10.

Weiss, R.F., 1974. Carbon dioxide in water and seawater: The solubility of a non-ideal gas. Mar. Chem. 2 (3), 203–215. https://doi.org/10.1016/0304-4203(74)90015-2.

Wickström, S., Jonassen, M.O., Vihma, T., Uotila, P., 2019. Trends in cyclones in the high-latitude North Atlantic during 1979–2016. Q. J. R. Meteorol. 1–18 https://doi.org/10.1002/qj.3707.

Wiedmann, I., Reigstad, M., Marquardt, M., Vader, A., Gabrielsen, T.M., 2016. Seasonality of vertical flux and sinking particle characteristics in an ice-free high arctic fjord – Different from subarctic fjords? J. Mar. Syst. 156, 192–205. https://doi.org/10.1016/j.jmarsys.2015.10.003.

Xie, J., Raj, R.P., Bertino, L., Samuelsen, A., Wakamatsu, T., 2019. Evaluation of Arctic Ocean surface salinities from the Soil Moisture and Ocean Salinity (SMOS) mission

against a regional reanalysis and in situ data. Ocean Sci. 15, 1191–1206. https://doi.org/10.5194/os-15-1191-2019.

Yasunaka, S., Murata, A., Watanabe, E., Chierici, M., Fransson, A., van Heuven, S., Hoppema, M., Ishii, M., Johannessen, T., Kosugi, N., Lauvset, S.K., Mathis, J.T., Nishino, S., Omar, A.M., Olsen, A., Sasano, D., Takahashi, T., Wanninkhof, R., 2016. Mapping of the air-sea CO_2 flux in the Arctic Ocean and its adjacent seas: Basin-wide distribution and seasonal to interannual variability. Polar Sci. 10, 323–334. https://doi.org/10.1016/j.polar.2016.03.006.

Yasunaka, S., Siswanto, E., Olsen, A., Hoppema, M., Watanabe, E., Fransson, A., Chierici, M., Murata, A., Lauvset, S.K., Wanninkhof, R., Takahashi, T., Kosugi, N., Omar, A.M., van Heuven, S., Mathis, J.T., 2018. Arctic Ocean CO_2 uptake: an improved multiyear estimate of the air-sea CO2 flux incorporating chlorophyll *a* concentrations. Biogeosciences 15, 1643–1661. https://doi.org/10.5194/bg-15-1643-2018.